# H+ Transport is an Integral Function of the Mitochondrial ADP/ATP Carrier

**Ambre M. Bertholet**[1], **Edward T. Chouchani**[2], **Lawrence Kazak**[2], **Alessia Angelin**[3], **Andriy Fedorenko**[1], **Jonathan Z. Long**[2], **Sara Vidoni**[2], **Ryan Garrity**[2], **Joonseok Cho**[4], **Naohiro Terada**[4], **Douglas C. Wallace**[3], **Bruce M. Spiegelman**[2], **Yuriy Kirichok**[1,*]

[1]Department of Physiology, University of California San Francisco, San Francisco, CA, USA

[2]Dana-Farber Cancer Institute & Department of Cell Biology, Harvard Medical School, Boston, MA, USA

[3]Center for Mitochondrial and Epigenomic Medicine, Children's Hospital of Philadelphia, Department of Pathology and Laboratory Medicine, University of Pennsylvania, Philadelphia, PA 19104, USA

[4]Department of Pathology, University of Florida College of Medicine, Gainesville, FL, USA

## SUMMARY

The mitochondrial ADP/ATP carrier (AAC) is a major transport protein of the inner mitochondrial membrane. It exchanges mitochondrial ATP for cytosolic ADP and controls cellular ATP production. In addition, AAC may mediate mitochondrial uncoupling, but this AAC function and its mechanisms remain elusive. Here we record AAC currents directly from inner mitochondrial membrane of various tissues and identify two distinct transport modes: ADP/ATP exchange and H$^+$ transport. The AAC-mediated H$^+$ current requires free fatty acids and resembles the H$^+$ leak via the thermogenic uncoupling protein 1 of brown fat. The ADP/ATP exchange via AAC negatively regulates the H$^+$ leak, but without complete inhibition. This suggests that the H$^+$ leak and mitochondrial uncoupling could be dynamically controlled by cellular ATP demand and the rate of ADP/ATP exchange. By mediating two distinct transport modes, ADP/ATP exchange and H$^+$ leak, AAC intimately connects coupled (ATP production) and uncoupled (thermogenesis) energy conversion in mitochondria.

## INTRODUCTION

AAC exchanges cytosolic and mitochondrial adenine nucleotides across the inner mitochondrial membrane (IMM) to provide ADP for ATP synthesis and deliver ATP into the cytosol[1]. Humans have four AAC isoforms, AAC1-AAC4 (AAC4 is specific to germ cells and pluripotent stem cells)[1-3]. Mice lack AAC[4,5]. AAC operates by the alternating access mechanism with a single substrate binding site (SBS) intermittently exposed to either cytosolic (c-state) or matrix (m-state) side of the IMM (Extended Data Fig. 8a)[1,6]. Additionally, two other roles, in mitochondrial uncoupling [7-10] and the permeability transition pore (PTP)[11,12], have been proposed for AAC.

Uncoupling proteins (UCPs) mediate $H^+$ leak ($I_H$) across the IMM. $I_H$ uncouples the $H^+$ flows via electron transport chain and the ATP synthase to reduce efficiency of ATP production and cause mitochondrial thermogenesis. $I_H$ also decreases reactive oxygen species (ROS) production, protecting mitochondrial integrity[8,13]. $I_H$ via UCPs is activated by free long-chain fatty acids (FA)[14]. UCP1 is the UCP of brown and beige fat[15-18], but the identity of UCP(s) responsible for $I_H$ in all other tissues has remained elusive. It was suggested that all ~50 members of the SLC25 superfamily of mitochondrial solute carriers can contribute to $I_H$[19], most notably the close UCP1 homologs UCP2 and UCP3[20-22], AAC[7-9], aspartate-glutamate carrier[8,23], dicarboxylate carrier[8,24], and phosphate carrier[25,26]. $I_H$ may also occur through the lipid phase without protein involvement [27]. With so many proposed $I_H$ pathways, the molecular mechanisms of mitochondrial uncoupling became challenging to comprehend.

The role of AAC in $I_H$ was further obscured by AAC implication in the permeability transition pore (PTP) of the IMM. PTP causes mitochondrial uncoupling and can lead to mitochondrial dysfunction and cell death[11,12,28]. Because FA also activate the PTP[27-31], it was unclear whether AAC contributes to FA-dependent mitochondrial uncoupling via a $H^+$-selective $I_H$ or non-selective PTP. Here we unravel the functional complexity of AAC by directly recording the transmembrane currents carried by AAC across the native IMM.

## RESULTS

### Identification of ubiquitous FA-dependent mitochondrial $I_H$

To characterize $I_H$ in tissues that do not express UCP1, we used the whole-IMM patch-clamp[17,18] (Extended Data Fig. 1a). Application of 1.5 μM arachidonic acid (AA) on the cytosolic side (bath) induced $I_H$ across the whole IMM of skeletal muscle (SM; Extended Data Fig. 1b), heart, liver, and brown fat (Extended Data Fig. 2a). $I_H$ reversed at the calculated $H^+$ Nernst potentials (Extended Data Fig. 3). Interestingly, a small $I_H$ appeared before AA addition that was inhibited by FA acceptor methyl-β-cyclodextrin (MβCD) and likely activated by FA within the IMM (Extended Data Fig. 2e).

It was proposed that FA possess protonophoric activity and cause $H^+$ current across any lipid bilayer, independent of transport proteins[27]. However, neither 1.5 μM nor 15 μM AA induced measurable currents across the plasma membrane but generated robust $I_H$ across the

IMM (Extended Data Fig. 1b-d). Thus, FA-dependent $I_H$ is not a universal property of lipid bilayers but a feature of the IMM.

We found no difference in $I_H$ amplitude in SM mitoplasts isolated from mice deficient for UCP2 and UCP3 as compared to WT (Extended Data Fig. 2b and c). Guanosine diphosphate (GDP), an inhibitor of UCPs[20-22,32], also had no effect on $I_H$ (Extended Data Fig. 2d). This finding correlates with the recently proposed roles of these proteins in mitochondrial transport of C4 metabolites and glucose/pyruvate metabolism, rather than mitochondrial uncoupling[33,34].

### Pharmacological and biophysical properties of I_H

At physiological pH (7.5/7.0 inside/outside of mitoplast), 2 μM AA induced both inward (observed at negative membrane voltages) and outward (at positive voltages) currents in SM, heart, kidney, and liver mitoplasts (Fig. 1a). This effect was reversible upon FA washout (Extended Data Fig. 4i). A specific AAC inhibitor carboxyatractyloside (CATR)[1] strongly inhibited the inward current but only partially the outward current (Fig. 1a and Extended Data Fig. 4k and l). Shorter chain palmitic acid (PA) and lauric acid induced similar CATR-sensitive currents (Extended Data Fig. 4a-c). Another selective AAC inhibitor, bongkrekic acid (BKA), also suppressed $I_H$ (Extended Data Fig. 4d).Thus, the CATR- and BKA-sensitive inward $I_H$ observed at physiologically relevant negative membrane potentials is likely mediated by AAC. In contrast, the largely CATR- and BKA-insensitive outward current observed at positive voltages is partially mediated by another transport mechanism.

We hypothesized that the outward current is mainly carried by FA anions as it was greatly reduced in a low pH bath solution with fewer cytosolic FA anions (Extended Data Fig. 1b, 2a, and 4j). To test this, we added 2 μM AA-sulfonate (AA-sulf, an AA analog that exists only in the unprotonated anionic form at physiological pH) to the bath and observed only an outward current, as expected for transport of negatively charged AA-sulf into the mitoplast (Extended Data Fig. 4e). Notably, this current was not affected by CATR (Extended Data Fig. 4e), ruling out AAC involvement. Sulfhydryl reagent mersalyl strongly inhibited the outward FA anion current induced by AA-sulf (Extended Data Fig. 4f) or AA (Extended Data Fig. 4g) but did not affect the inward $I_H$ induced by AA (Extended Data Fig. 4g), further confirming that different proteins carry the AA anion and $H^+$ currents induced by AA. Mersalyl washout did not restore the outward AA anion current, whereas dithiothreitol (DTT) addition did (Extended Data Fig. 4h), suggesting cystein oxidation involvement. Pre-treatment with mersalyl before AA application allowed measuring the AAC-dependent $I_H$ in isolation (Fig. 1b). The outward $I_H$ via AAC was smaller than the inward $I_H$ due to the inward $H^+$ gradient used in this experiment (Fig. 1b). In this study, we avoided using mersalyl and measured AAC-dependent $I_H$ in isolation from the AAC-independent FA anion current either at negative potentials or low pH.

In the absence of purine nucleotides that negatively regulate $I_H$ via both UCP1 and AAC (Fig. 4 and Extended Data Fig. 9d-f), the density of the AAC-dependent $I_H$ was about ~5 times smaller than that of the UCP1-dependent $I_H$ (Fig. 1b-d).

Mitochondrial uncoupling is potentiated by both mitochondrial hyperpolarization and ROS, which serve as a negative feedback mechanism for mitochondrial ROS production[13,35-37]. Accordingly, the current–voltage relationship of the AAC-dependent $I_H$ was non-linear, with $I_H$ increasing sharply with membrane hyperpolarization (Fig. 1e and f). Also, application of *tert*-butyl hydroperoxide (tBHP), tributyltin (TBT), or 4-hydroxynonenal (4-HNE), known to oxidize AAC cysteines[38,39], on the cytosolic face of the IMM significantly potentiated $I_H$ via AAC (Extended Data Fig. 5a, c, and e). Importantly, because tBHP, TBT, and 4-HNE activated no currents in the absence of FA (Extended Data Fig. 5b, d, and f), they do not act independently but potentiate the FA-induced $I_H$.

Thus, pharmacological evidence suggests that AAC is responsible for the FA-induced mitochondrial $I_H$. Importantly, low micromolar FA are required for $I_H$ via both AAC and UCP1[17]. Previous suggestions that UCP1 or AAC mediate a "basal" $I_H$ that is FA-independent[10] or activated by nanomolar FA concentrations[40] were likely associated with the inabilty to reliably control FA concentrations in mitochondrial respiration experiments[41].

## AAC is required for $I_H$

In mice, AAC1 and AAC2 are the only somatic isoforms[3,4]. AAC1 expression is highest in heart and SM, and AAC2 – in kidney[4,42]. In heart of $AAC1^{-/-}$ mice[5,43], AA failed to induce $I_H$ at negative potentials in all mitoplasts tested except one (Fig. 2a). The $I_H$ reduction was also drastic in $AAC1^{-/-}$ SM (Fig. 2b), with some mitoplasts having no $I_H$, while the remaining $I_H$ in others was still inhibited by CATR, suggesting AAC2 involvement (Fig. 2b, and Extended Data Fig. 6i and j). $I_H$ in kidney (where AAC1 expression is low[4]) was not significantly affected in $AAC1^{-/-}$ and remained CATR-sensitive (Fig. 2c). $I_H$ was not significantly altered in heart or kidney of $AAC2$ hypomorphic mice[42] (Extended Data Fig. 6a and b), and was CATR-sensitive likely due to compensation with AAC1[42] (Extended Data Fig. 6a and b). In contrast to $I_H$, the outward current observed at positive potentials (primarily the AAC-independent FA anion current) was still present in both $AAC$-deficient mice in all tissues tested (Fig. 2 and Extended Data Fig. 6a-g). This current was partially inhibited by 1 µM CATR (Extended Data Fig. 6h), but short of full inhibition expected for the current mediated only by AAC[1].

Thus, AAC1 plays a crucial role in $I_H$, at least in heart and SM. However, the recording of a CATR-sensitive $I_H$ in SM and kidney of $AAC1^{-/-}$ mice suggests that AAC2 is capable of mediating $I_H$.

## FA as co-factors for H$^+$ transport by AAC

In UCP1, $I_H$ activation requires FA binding within the translocation pathway[17]. The FA binding is facilitated by a longer carbon chain and higher FA hydrophobicity[17,44]. The protonatable carboxylic group of the FA located within the translocation pathway enables H$^+$ transport. Nonprotonatable low-pKa FA analogs (such as alkylsulfonales) inhibit $I_H$ by competing with FA for binding to UCP1[17,44]. Purine nucleotides, blockers of the UCP1 translocation pathway, abolish $I_H$ via UCP1[17,44].

The mechanism of $I_H$ via AAC appears to be similar. Blocking the AAC translocation pathway with CATR or BKA abolished $I_H$ (Fig. 1a and Extended Data Fig. 4d). Higher FA

hydrophobicity facilitated $I_H$ activation (Extended Data Fig. 4a-c). Finally, AA-sulf failed to induce $I_H$ (Extended Data Fig. 4e) but inhibited the $I_H$ activated by AA (Extended Data Fig. 7a).

However, UCP1 transport both, $H^+$ and FA, and operates as a FA anion/$H^+$ cotransporter[17,18,44,45]. The FA anion transport can be studied in isolation from $I_H$ using alkylsulfonates[17,44]. Short-chain alkylsulfonates (e.g., C6-sulf) are transported by UCP1 and induce a steady outward transmembrane current (Extended Data Fig. 7d, left panel)[17,44]. In contrast, long-chain alkylsulfonates (e.g., AA-sulf) cannot dissociate from UCP1 due to strong hydrophobic interactions but move within the translocation pathway in response to voltage steps, giving rise to transient currents (Extended Data Fig. 7c, left panel)[17,18,44]. However, neither AA- nor C6-sulf induced measurable AAC currents under these conditions (Extended Data Fig. 7c and d, right panels). Our attempts to induce FA anion currents via AAC by applying AA-sulf or C6-sulf on both sides of the IMM also resulted in no measurable FA anion currents (Extended Data Fig. 7e and f). However, at higher voltage (−160 mV), we detect a small transient current likely generated by AA-sulf trapped within AAC translocation pathway (Extended Data Fig. 7c, left panel). In contrast, AA induced a steady $I_H$ under the same conditions (Extended Data Fig. 7b).

Thus, the presence of protonatable FA within the translocation pathway appears to be the common feature in FA-dependent $H^+$ transport by AAC and UCP1. However, FA serve as cofactors[41] in $H^+$ translocation by AAC , not co-transported species[17] as for UCP1 (Extended Data Fig. 7g).

### Adenine nucleotide transport by AAC

We next recorded AAC currents associated with the exchange of $Mg^{2+}$-free ADP and ATP (Extended Data Fig. 8a). Application of 1 mM ADP on the cytosolic IMM face, while the matrix solution contained 1 mM ATP, resulted in a small CATR-sensitive current (Extended Data Fig. 9b). The current increased significantly in 5 mM [ATP] and [ADP] and, as expected for electrogenic exchange of cytosolic $ADP^{3-}$ for matrix $ATP^{4-}$, was observed only in the inward direction at negative voltages (Fig. 3a, left panel and Extended Data Fig. 8c). This current was dramatically reduced in $AAC1^{-/-}$ heart mitoplasts (Fig. 3a and d). With matrix ADP and cytosolic ATP, the current reversed and was only observed in the outward direction at positive voltages (Fig. 3b and Extended Data Fig. 8d). Finally, 5 mM ADP on both IMM sides resulted in no current (Fig. 3c), as expected for homoexchange[1]. The ability to measure ADP/ATP exchange and control AAC conformations with the patch-clamp technique provided further insight into the mechanism of FA-dependent $I_H$.

Nearly all AAC molecules in isolated mitoplasts were initially in the c-state (see Methods), because CATR, a c-state–specific AAC inhibitor[1,46], almost completely blocked FA-dependent $I_H$ (Fig. 1a and Extended Data Fig. 4k). Interestingly, pre-treatment of a mitoplast with cytosolic ADP to induce an m-state transition of the AAC molecules did not prevent subsequent activation of $I_H$ with FA but, made $I_H$ insensitive to CATR (Fig. 3e and Extended Data Fig. 8e). Thus, $I_H$ inhibition by the c-state–specific inhibitor CATR allows identification of AAC conformational states during patch-clamp experiments. This experiment demonstrates that: 1) cytosolic FA activate $I_H$ with AAC in either the c- or m-

state; 2) FA cannot induce the c–m conformational change (only adenine nucleotides can) and are not AAC transport substrates (see also Extended Data Fig. 7c-f).

Interestingly, 4 μM of matrix AA did not activate $I_H$ when AAC was either in the c-state (Extended Data Fig. 8f) or m-state (after treatment with cytosolic ADP, Extended Data Fig. 8g), but subsequent addition of 2 μM AA on the cytosolic side activated robust $I_H$. Therefore, similar to UCP1[17], FA only bind to AAC on the cytosolic face of the IMM.

Thus, AAC has two transport modes: the electrogenic ADP/ATP exchange that relies on the c–m conformational change (Extended Data Fig. 8a) and $I_H$ that is activated by cytosolic FA independently of the AAC conformation (Extended Data Fig. 7g).

### Nucleotide exchange negatively regulates $I_H$

Application of ADP only on the cytosolic face of the IMM induced transient and partial $I_H$ inhibition (Fig. 4a and c). Such transient inhibition likely occurred because cytosolic ADP caused transient ADP transport and thus only briefly obstructed the translocation pathway for $I_H$ (Extended Data Fig. 9a). Addition of 1 mM ADP on both IMM sides to activate continuous adenine nucleotide exchange via AAC led to steady (but still partial) inhibition of $I_H$ (Fig. 4b and d, and Extended Data Fig. 9b). Symmetrical addition of 100 μM ADP caused smaller $I_H$ inhibition, while 10 μM ADP had no effect (Extended Data Fig. 9c).

Interestingly, the same ADP concentrations more profoundly inhibited $I_H$ via UCP1 as compared to AAC. For example, 100 μM ADP inhibited $I_H$ via UCP1 by >10-fold, compared to an ~2-fold inhibition of $I_H$ via AAC (Fig. 4e and Extended Data Fig. 9d-f). The stronger inhibition of UCP1 is likely because adenine nucleotides are not transported species but blockers of UCP1. Thus, despite a higher $H^+$-transport capacity of UCP1 (Fig. 1d), adenine nucleotides make $I_H$ via UCP1 and AAC comparable in amplitude, suggesting their closer impact on mitochondrial uncoupling in situ.

In conclusion, $I_H$ via AAC is reduced, but not fully inhibited, by adenine nucleotide exchange. The two transport modes of AAC appear to compete and likely occur via overlapping translocation pathways.

### AAC deficiency disrupts mitochondrial uncoupling

In agreement with the dramatically reduced $I_H$ in $AAC1^{-/-}$ mouse heart mitoplasts (Fig. 2a), FA-induced uncoupled respiration was completely disrupted in isolated heart mitochondria of $AAC1^{-/-}$ mice (Fig. 5a and Extended Data Fig. 10a). The basal respiration of $AAC1^{-/-}$ mitochondria was slightly greater than that of WT mitochondria (Extended Data Fig. 10a and b), likely due to their greater exposure to oxidative stress in vivo and susceptibility to PTP activation[43,47].

We then generated a C2C12 mouse cell line deficient for AAC1 and AAC2 (*AAC1/AAC2* double knockout, DKO). The abundances of mitochondrial respiratory complexes and ATP synthase, the mitochondrial morphology, mitochondrial biomass per cell, and mitochondrial DNA abundance were overall similar in WT and DKO cells (Extended Data Fig. 10c and e-g). Isolated DKO mitochondria had disrupted ADP-dependent respiration (Extended Data

Fig. 10d). The DKO cells were more glycolytic and demonstrated a higher extracellular acidification rate than WT cells (Extended Data Fig. 10h). Strikingly, the basal respiration of isolated DKO mitochondria was dramatically reduced both in the presence (Fig. 5b) and in the absence (Extended Data Fig. 10d) of the ATP synthase inhibitor oligomycin, which illustrates that FA-dependent $I_H$ via AAC, strongly contributes to mitochondrial uncoupling. PA-induced uncoupled respiration was also disrupted in isolated DKO mitochondria (Fig. 5c). However, gramicidin A stimulated respiration to a similar degree in DKO and WT mitochondria confirming intact respiratory capacity of DKO mitochondria (Fig. 5b).

Intact DKO cells had a significantly reduced basal respiration rate (Fig. 5d), which was expected because their mitochondria support neither ADP-dependent nor uncoupled respiration (Extended Data Fig. 10d and Fig. 5b). Importantly, the respiration rates of WT and DKO cells with oligomycin treatment still differed significantly (Fig. 5d), demonstrating severe disruption of uncoupled respiration in intact DKO cells. Finally, sequentially higher PA concentrations failed to increase uncoupled respiration of DKO cells (Fig. 5e).

Together, these data demonstrate that disruption of the AAC-dependent $I_H$ profoundly affects mitochondrial uncoupling in isolated mitochondria and intact cells.

## DISCUSSION

Our data suggest that AAC is responsible for mitochondrial $I_H$ in all tissues that do not express UCP1. The principal characteristics of $I_H$ mediated by AAC and UCP1 are similar, with FA being activators and purine nucleotides being negative regulators. Our data argue against the notions that close UCP1 homologs, UCP2 and UCP3, and all other SLC25 family members contribute to FA-dependent $I_H$. If they did, we would detect significant AAC-independent $I_H$ in patch-clamp experiments, but we do not. We also did not identify large PTP-like channels/pores possibly formed by AAC, but the AAC-dependent $I_H$ may facilitate PTP opening by inducing mitochondrial depolarization, a key PTP activator[11,12].

It was previously suggested that AAC can mediate FA-independent "basal" $I_H$[10], but our data demonstrate that FA are required for H$^+$ transport via AAC. In fact, the presence of protonatable FA within the translocation pathway is the common requirement for $I_H$ via both AAC and UCP1. However, unlike with UCP1, FA appear to bind within the AAC translocation pathway as co-factors rather than transport substrates. Mitochondria of various tissues possess phospholipase A2 activity[17,18,48,49], which may be the primary physiological source of FA for AAC-dependent $I_H$.

With AAC, $I_H$ is negatively regulated by ADP/ATP exchange, whereas with UCP1, $I_H$ is simply inhibited by cytosolic adenine nucleotides. This ability to dynamically adjust $I_H$ in accordance with ADP/ATP exchange (and thus cellular ATP demand) could make AAC uniquely suited to be the UCP of mitochondria that specialize in ATP production. Thus, AAC appears to serve as a master regulator of mitochondrial energy output, maintaining a delicate balance between ATP production and thermogenesis.

# METHODS

## Animals

Mice were maintained on a standard rodent chow diet under 12-h light and dark cycles. All animal experiments were performed with male mice (2 months – 1 year of age) according to procedures approved by the UCSF Institutional Animal Care and Use Committee. B6.129-Ucp1tm1Kz/J mice (abbreviated *UCP1⁻/⁻*), B6.129S4-Ucp2tm1Lowl/J mice (abbreviated *UCP2⁻/⁻*) and B6;129S4-Ucp3tm1Lowl/J mice (abbreviated *UCP3⁻/⁻*) were obtained from the Jackson Laboratory. The Ant2SIBN 129/B6 mice (abbreviated AAC2 hypomorphic) were provided by the laboratory of Dr. Naohiro Terada[42], and AAC1-deficient mice on C57BL/6J2z background were obtained from the laboratory of Dr. Douglas Wallace[5]. Sample size was chosen based on results of pilot experiments to ensure statistical significance could be reached. Randomization was not performed because mice were grouped based on genotype. Blinding was not used.

## Isolation of mitochondria and mitoplasts from tissues

Mice were sacrificed by $CO_2$ asphyxiation followed by cervical dislocation. For the preparation of mitoplasts from heart, SM, brown fat, kidney, and liver, the selected mouse tissues were isolated, rinsed, and homogenized in ice-cold medium containing 250 mM sucrose, 10 mM HEPES, 1 mM EGTA, and 0.1% bovine serum albumin (BSA) (pH adjusted to 7.2 with Trizma® base) using a glass grinder with six slow strokes of a Teflon pestle rotating at 275 (soft tissues) or 600 (fibrous tissues) rotations per minute. The homogenate was centrifuged at 700 x g for 5–10 min to pellet nuclei and unbroken cells. For some tissues, the first nuclear pellet was resuspended in the same solution and homogenized again to increase the yield of mitochondria. Mitochondria were collected by centrifugation of the supernatant at 8,500 x g for 10 min.

Mitoplasts were produced from mitochondria using a French press. Briefly, mitochondria were suspended in a solution containing 140 mM sucrose, 440 mM D-mannitol, 5 mM HEPES, and 1 mM EGTA (pH adjusted to 7.2 with Trizma® base) and then subjected to a French press at 1200–2,000 psi to rupture the outer membrane. Mitoplasts were pelleted at 10,500 x g for 15 min and resuspended for storage in 500 μl of solution containing 750 mM KCl, 100 mM HEPES, and 1 mM EGTA (pH adjusted to 7.2 with Trizma® base). Mitochondria and mitoplasts were prepared at 0–4 °C and stored on ice for up to 5 h. Immediately before the electrophysiological experiments, 15–50 μl of the mitoplast suspension was added to 500 μl solution containing 150 mM KCl, 10 mM HEPES, and 1 mM EGTA (pH adjusted to 7.0 with Trizma® base) and plated on 5-mm coverslips pretreated with 0.1% gelatin to reduce mitoplast adhesion. Nearly all AAC molecules in isolated mitoplasts were initially in the c-state (see Fig. 1a and 3e). A likely explanation for this initial c-state is the presence of endogenous adenine nucleotides in the matrix and not in the isolation media during mitochondria/mitoplast isolation.

## Patch-clamp recordings

Patch-clamp recording was performed from isolated mitoplasts. The mitoplasts used for patch-clamp experiments were 3–5 μm in diameter and typically had membrane

capacitances of 0.3–1.2 pF. Gigaohm seals were formed in the bath solution containing 150 mM KCl, 10 mM HEPES, and 1 mM EGTA (pH 7 adjusted with Trizma® base). Voltage steps of 250–500 mV and 1–50 ms were applied to break-in into the mitoplast and obtain the whole-mitoplast configuration (Extended Data Fig. 1a), as monitored by the appearance of capacitance transients. Mitoplasts were stimulated every 5 s. Currents were normalized per membrane capacitance to obtain current densities (pA/pF).

All indicated voltages are on the matrix side of the IMM (pipette solution) as compared to the cytosolic side (bath solution, defined to be 0 mV). Normally, currents were induced by a voltage ramp from −160 mV to +100 mV to cover all physiological voltages across the IMM, but other voltage protocols were also used as indicated in the figures. Currents flowing into mitochondria are shown as negative, while those flowing out are positive (Extended Data Fig. 1). Membrane capacitance transients observed upon application of voltage steps were removed from current traces.

Both the bath and pipette solutions were formulated to record $H^+$ currents and contained only salts that dissociate into large anions and cations normally impermeant through ion channels or transporters. In the majority of experiments, we used a low pH gradient across the IMM (pH 7.5 and 7.0 on the matrix and cytosolic sides, respectively) to approximate physiological conditions. However, other pH gradients were also used as indicated.

Pipettes were filled with 130 mM tetramethylammonium hydroxide (TMA), 1.5 mM EGTA, 2 mM Tris chloride, and 100 mM HEPES (or MES). pH was adjusted to 6-7.5 with D-gluconic acid, and tonicity was adjusted to ~360 mmol/kg with sucrose. Typically, pipettes had resistances of 25–35 MΩ, and the access resistance was 40–75 MΩ.

Whole-mitoplast $I_H$ was recorded in the bath solution containing 100 mM HEPES (or MES) and 1 mM EGTA (pH adjusted to 6.0–7.5 with Trizma® base, and tonicity adjusted to ~300 mmol/kg with sucrose). AA was selected as the $I_H$ activator, because this polyunsaturated FA is a principal product of membrane phospholipid hydrolysis[50]. In the absence of significant cytosolic triglyceride storage in non-adipose tissues, membrane phospholipid hydrolysis may be an important source of free FA for $I_H$ activation in vivo[17,48]. To record UCP1 currents, before the application of AA, the endogenous membrane FA were removed by a 30-40s pre-treatment with 10 mM MβCD[17]. Low pH 6.0 was employed in some UCP1 experiments to further suppress production of endogenous FA in brown fat mitoplasts[17].

All experiments were performed under continuous perfusion of the bath solution. All electrophysiological data presented were acquired at 10 kHz and filtered at 1 kHz.

### Mitochondrial respiration on isolated heart mitochondria

After mitochondria were isolated from WT and $AAC1^{-/-}$ hearts (5 months old, 3-4 mice per genotype) as described above. The organelles were rinsed with a BSA-free isolation buffer (250 mM sucrose, 10 mM HEPES, 1 mM EGTA, pH adjusted to 7.2 with Trizma® base) to remove the BSA. Mitochondrial oxygen consumption rates (OCRs) were evaluated in heart isolated mitochondria using the Seahorse XF24 Analyzer (Seahorse Bioscience, Billerica, MA). The experiments were performed with respiratory buffer (sucrose 70 mM, mannitol

220 mM, potassium phosphate monobasic 10 mM, magnesium chloride 5 mM, HEPES 2 mM, EGTA 1 mM, glutamate 10 mM, and malate 2 mM) supplemented with 0.02% FA-free BSA. Mitochondrial protein was quantified using Bradford protein assay. We used 5 μg of mitochondrial proteins per well. The mitochondrial respiration was measured before any addition (basal), then after addition of 4 μg/ml oligomycin (Oligo), followed by 50 μM or 100 μM palmitic acid (PA) or respiration buffer to study the $H^+$ leak, and then after addition of 0.1 μM FCCP to induce maximal respiration. Finally, 1 μM rotenone was applied to inhibit mitochondrial respiration. In each experiment, 2-3 wells were left unseeded for the collection of background measurements. Each experimental condition was applied to 3-4 wells per plate and repeated over 3-4 days (independent mitochondrial isolation). Basal respiration was measured at three consecutive time points; the effect of oligomycin was measured at two consecutive time points; the effect of FA was measured at nine consecutive time points (30 min total); and the effects of FCCP and rotenone were measured at one or two consecutive time points. The OCRs immediately after the addition of PA and after 30 min are reported.

### C2C12 cell culture and AAC1/AAC2 knockout generation

The C2C12 cell line was purchased from ATCC (https://www.atcc.org/) and cultured in complete Dulbecco's Modified Eagle Medium (DMEM; DMEM with 25 mM Glucose, 10% fetal bovine serum [FBS], penicillin and streptomycin antibiotics). The C2C12 cell line was authenticated by ATCC. The *AAC1/AAC2* DKO C2C12 cells were generated by Alstem LLC (http://www.alstembio.com/) using the Crispr-Cas9 system. Alstem LLC provided initial authentification of *AAC1/AAC2* DKO C2C12 cells with PCR. We provided further authentication of the DKO cells with western blotting and patch-clamp electrophysiology . All cell lines were tested negative for mycoplasma contamination by Alstem LLC. Transfection of gRNA Cas9 plasmids was performed using the Invitrogen Neon transfection system. gRNA candidates were selected via PCR amplification and selected for single-cell clone isolation.

AAC1 gRNA target 1 "CGCCGCCGTCTCCAAGACGG CGG" and target 2 "GGGGCGGGGCGCGCGCGCGTCA GGG"

AAC2 gRNA target 1 "CGGCTTTGACTCCCGGGCTC TGG" and target 2 "AGGTACGTTCTGAGATCGAG GGG". Because DKO cells were glycolytic (Extended Data Fig. 10h), growing them in a low-glucose medium would put DKO cells at a significant disadvantage as compared to WT cells, effectively resulting in vastly different growing conditions for the two cell lines. Therefore, the same growth medium containing 25 mM glucose was used for both for WT and DKO cells.

### Immunocytochemistry

C2C12 cells were seeded on 2-cm diameter coverslips in a multi-well plate. For immunostaining, cells were fixed in 3.7% paraformaldehyde for 20 min at 37°C and permeabilized in 0.5% Triton X-100 for 10 min at room temperature. A 2-h incubation in primary rabbit polyclonal anti-TOM20 (Santa Cruz Biotechnology: FL-145) and mouse monoclonal anti-tubulin antibodies (Abcam: A44928) both diluted at 1:500 was followed by

incubation in solution containing the secondary antibodies Alexa Fluor 488-conjugated goat anti-rabbit (Invitrogen: A11008) and Alexa Fluor 568-conjugated goat anti-mouse (Invitrogen: A11004) for 1 h at room temperature. The coverslips were mounted onto a cover glass using Prolong mounting medium (Invitrogen: P36934). Images were acquired using a Yokogawa CSU-X1 spinning disk confocal on an inverted Nikon Ti fluorescence microscope equipped with a 63× or 100× oil immersion objective. Image analysis and processing were performed using the NIS Elements software on 0.2-μm z-stack images acquired with the 100× objective. To quantify mitochondrial area, the maximum-intensity projections labeled with TOM20 on each acquired z-stack image were used.

## C2C12 mitochondrial isolation

C2C12 cells (WT or DKO) from ten 15-cm dishes were trypsinized and harvested with ice-cold PBS at 1,000 g for 5 min. The cell pellet was incubated with hypotonic buffer (20 mM HEPES, pH 7.5, 5 mM KCl, 1.5 mM $MgCl_2$, and 1 mg/ml essentially FA-free BSA) on ice for 10 min. Cells were then homogenized (25 strokes) using a tight-fitting glass dounce tissue grinder and rapidly made isotonic by adding the homogenate to 2/3 volume of 2.5x MSH (20 mM HEPES, pH 7.5, 525 mM mannitol, 175 mM sucrose, 5 mM EDTA, and 1 mg/ml essentially FA-free BSA). The homogenate was centrifuged at $600 \times g$ for 10 min, and the supernatant was then centrifuged at $8,500 \times g$ for 10 min to pellet mitochondria. Mitochondria were resuspended in MSH buffer (20 mM HEPES, pH 7.5, 210 mM mannitol, 70 mM sucrose, and 2 mM EDTA). Mitochondrial protein was quantified using the bicinchoninic acid assay (Thermo Fisher Scientific).

## Extracellular flux analysis of C2C12 cell-derived mitochondria

In a volume of 50 μl, 30 μg of mitochondrial protein was added to each well of a XF cell culture microplate (on ice). The mitochondria-loaded XF microplate was centrifuged at $2,000 \times g$ for 20 min for adherence of organelles. Respiration buffer (20 mM Tris, pH 7.4, 210 mM mannitol, 70 mM sucrose, 0.1 mM EGTA, 3 mM $MgCl_2$, 5 mM $KH_2PO_4$, 0.1% essentially FA-free BSA, 10 mM sodium pyruvate, and 5 mM malate) was added to a final volume of 0.5 ml, and the XF microplate was warmed at 37 °C for 8 min prior to loading into a XFe24 Extracellular Flux Analyzer (Seahorse Bioscience). The OCRs were recorded using a mix (20 s) and measure (2 min) cycle. FCCP was added at 10 μM (isolated mitochondria). Gramicidin A was added at 10μM.

## Extracellular flux analysis of cultured C2C12 cells

Cells were plated in an XF microplate the evening before respirometry at 60,000 cells or 50,000 per well. Cells were washed with 250 μl unbuffered DMEM (Sigma, D5030), supplemented with 0.2% and 1 mM sodium pyruvate. Then 600 μl of unbuffered DMEM (supplemented with 0.2% and 1 mM sodium pyruvate) was added to the cells before incubation at 37 °C without $CO_2$ for 45 min. The OCRs were recorded using a mix (3 min), wait (2 min), and measure (3 min) cycle. The final concentrations of palmitate were 200, 400, or 600 μM, and that of FCCP was 4 μM.

### Analysis of mtDNA/nDNA ratio from C2C12 cells with quantitative PCR (qPCR)

After collecting ~5 million cells (WT and DKO, n=6), global DNA (including genomic and mitochondrial DNA) was extracted using the QIAamp DNA Mini Kit (ID: 51304 from Qiagen). We proceed to a serial 1/10-fold dilution of a WT sample for all the standard curves. Each sample has been diluted with a 1/5 ratio (genomic target, forward FWD: 5'-GCCAGCCTCTCCTGATTTTAGTGT-3' and reverse primers REV: 5'-GGGAACACAAAAGACCTCTTCTGG-3') and one mtDNA target (ND1 forward FWD: 5'-CTAGCAGAAACAAACCGGGC-3' and reverse primers REV: 5'-CCGGCTGCGTATTCTACGTT-3'). 1 µl of DNA and final concentration of 0.2 µM of each primer were mixed with Power SYBR Green Master Mix (Thermo Fisher Scientific) according to manufacturer's protocol. We normalized all our expression values to the expression of the genomic target.

### Immunoblots

For western blot analysis, cells were lysed in RIPA buffer (1% Igepal, 0.1% sodium dodecyl sulfate, 0.5% sodium deoxycholate, 150 mM NaCl, 1 mM EDTA, 50 mM Tris-HCl (pH 7.4) and a cocktail of proteases inhibitors. Lysates were resolved by SDS-PAGE; transferred to PVDF membrane (Millipore); and probed with anti-Na$^+$/K$^+$-ATPase antibody (Abcam, ab76020), anti-TOM20 (Santa Cruz, sc-11415), OXPHOS cocktail (Abcam, ab110413), anti-AAC1 (ab102032) and anti-AAC2 (CST 1467S).

### Chemicals

The following chemicals were used in this study: arachidonic acid sodium salt (AA, SIGMA A8798), palmitic acid (PA, SIGMA P0500), sodium dodecanoate (LA, SIGMA L9755), carboxyatractyloside potassium salt (CATR, SIGMA 4992), Bongkrekic acid triammonium salt (BKA, Millipore 203671), guanosine 5′-diphosphate tris salt (GDP, SIGMA G7252), adenosine 5′-diphosphate sodium salt (ADP, SIGMA A2754), adenosine 5′-triphosphate disodium salt hydrate (ATP, SIGMA A6419), methyl-β-cyclodextrin (MβCD, SIGMA C4555), mersalyl acid (SIGMA M9784), arachidonic acid sulfonate sodium salt (AA-sulf, CAYMAN 9001886), 1-hexadecanesulfonic acid sodium salt (C6-sulf, SIGMA 106410), Gramicidin A (Abcam ab144510), DL-Dithiothreitol solution (DTT, SIGMA 646563). *Tert*-butyl hydroperoxide solution (tBHP, SIGMA 416665), 4-hydroxy nonenal (4-HNE, CAYMAN 75899-68-2), and tributyltin chloride (TBT, SIGMA T50202).

### Statistical analysis

Data are presented as mean ± SEM as specified in the figure legend. Statistical analysis was performed using software GraphPad Prism 8. Statistical significance with exact p value was determined with the method used as indicated in corresponding figure legend.

## DATA AVAILABILITY STATEMENT

All data used to support the conclusions of this study are included in this Article. Full all-point electrophysiological traces are available from the corresponding author upon request.
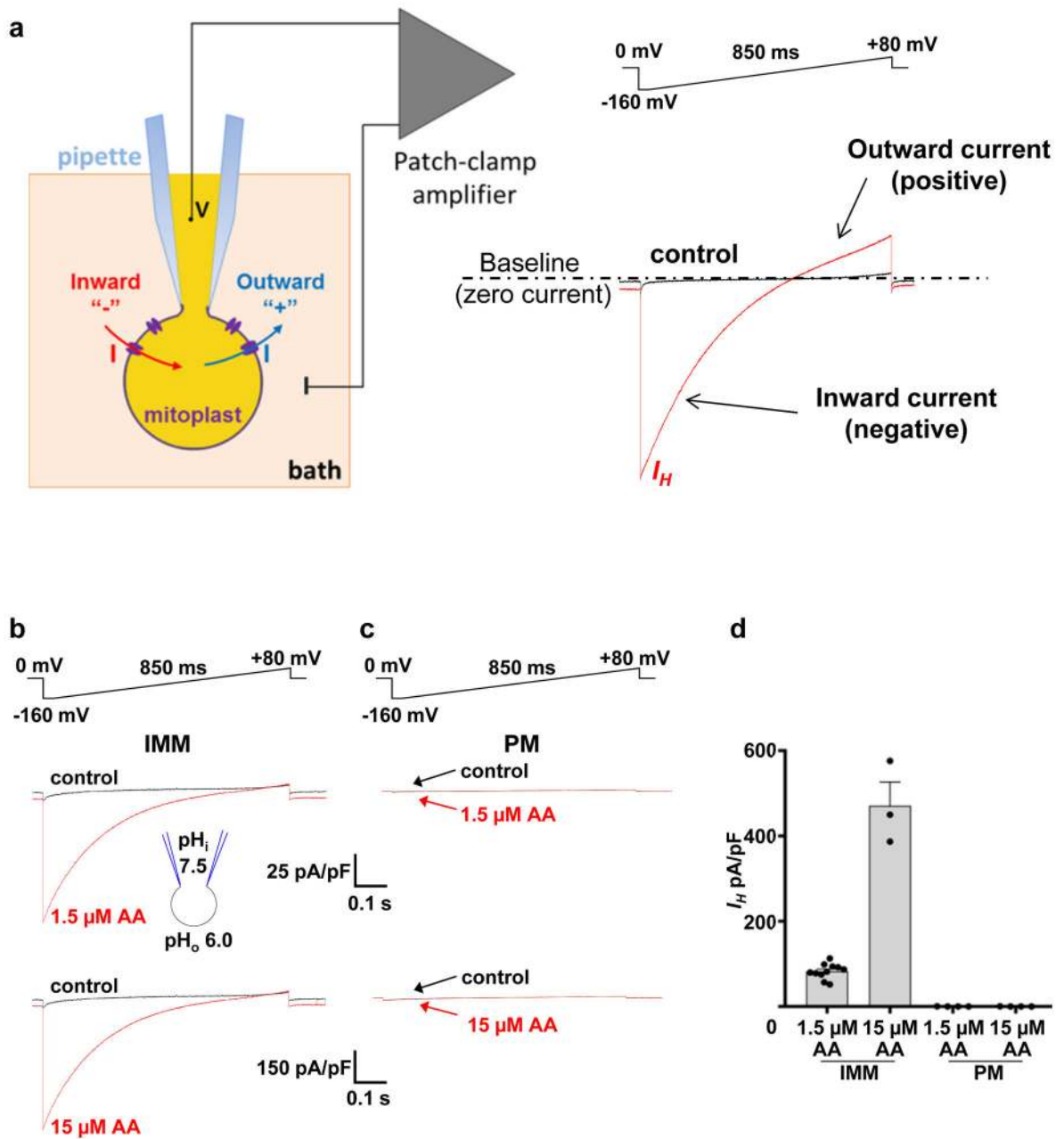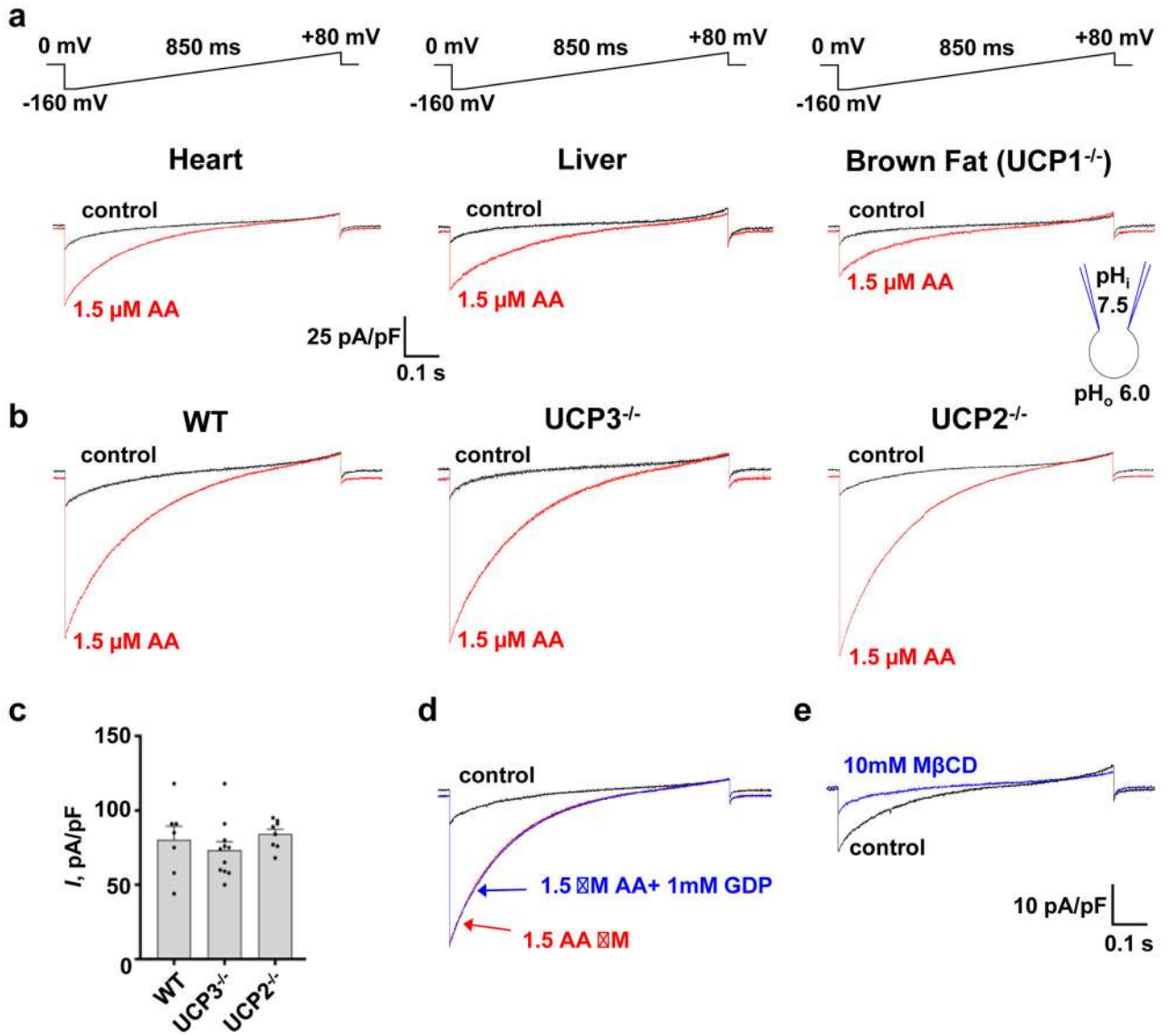
**Extended Data**

**Extended Data Figure 1 |. FA-dependent $I_H$ in the IMM and plasma membrane.**

**a,** *Left panel*: a diagram of patch-clamp recording from a vesicle of the whole IMM (mitoplast). After forming a gigaohm seal between the patch pipette and the mitoplast, the IMM patch under the pipette is broken by applying short pulses of high voltage (200–500 mV, 5-30 ms) combined with light suction to gain access into the mitoplast through the pipette. In this configuration, called the "whole-mitoplast" configuration, the interior of the mitoplast (mitochondrial matrix) is perfused with the pipette solution. The bath is also perfused to control the experimental solution on the cytosolic side of the IMM. The voltage across the IMM is set using the patch-clamp amplifier. Directions of currents flowing across the IMM: inward currents (flowing into the mitoplast) are negative, while outward currents

are positive. *Right panel:* an example of a $I_H$ current trace recorded in the whole-mitoplast mode. The voltage protocol used to induce the currents is shown above. All indicated voltages are within the mitochondrial matrix relative to the bath (cytosol). The voltage of the bath solution is defined to be zero. Baseline (zero current level) as well as negative (inward) and positive (outward) currents are indicated. **b,** $I_H$ induced in a SM mitoplast by 1.5 μM (IMM, upper panel, n=11) or 15 μM (IMM, lower panel, n=3) AA. Voltage protocol is shown above the traces. Bath (cytosolic side of the IMM) and pipette (matrix side) pH are indicated in the pipette-mitoplast diagram. **c,** Same experiment performed in the plasma membrane (PM, n=4 at 1.5 μM, n=4 at 15 μM) of HEK293 cells. **d,** $I_H$ densities in the IMM of SM and PM of HEK293 cells at 1.5 (n=11 for IMM, n=4 for PM) and 15 μM AA (n=3 for IMM, n=4 for PM). $I_H$ measured at −160 mV. Data represent mean±SEM.

**Extended Data Figure 2 |. UCP1-independent $I_H$ in various mouse tissues.**
**a**, $I_H$ induced in mitoplasts of heart (n=6), liver (n=5), and brown fat (*UCP1−/−* mice, n=6) by application of 1.5 μM AA on the cytosolic side of the IMM. Voltage protocol is shown above the traces. Bath and pipette pH are indicated in the pipette-mitoplast diagram. **b**, $I_H$ induced in mitoplasts of skeletal muscle (SM) of wild-type (WT, n=7), *UCP2−/−* (n=8), and *UCP3−/−* (n=11) mice by application of 1.5 μM AA on the cytosolic side of the IMM. **c**, $I_H$ densities in SM mitoplasts of WT (n=7), *UCP2−/−* (n=8), and *UCP3−/−* (n=11) mice, measured at −160 mV as in (b). Data represent mean±SEM. **d**, Representative SM mitochondrial $I_H$ induced by 1.5 μM AA before (red) and after application of 1 mM GDP (blue) (n=4). **e**, Mitochondrial $I_H$ recorded in the absence of added FA (control, black) was deactivated by addition of 10 mM MβCD to the bath (n=10).
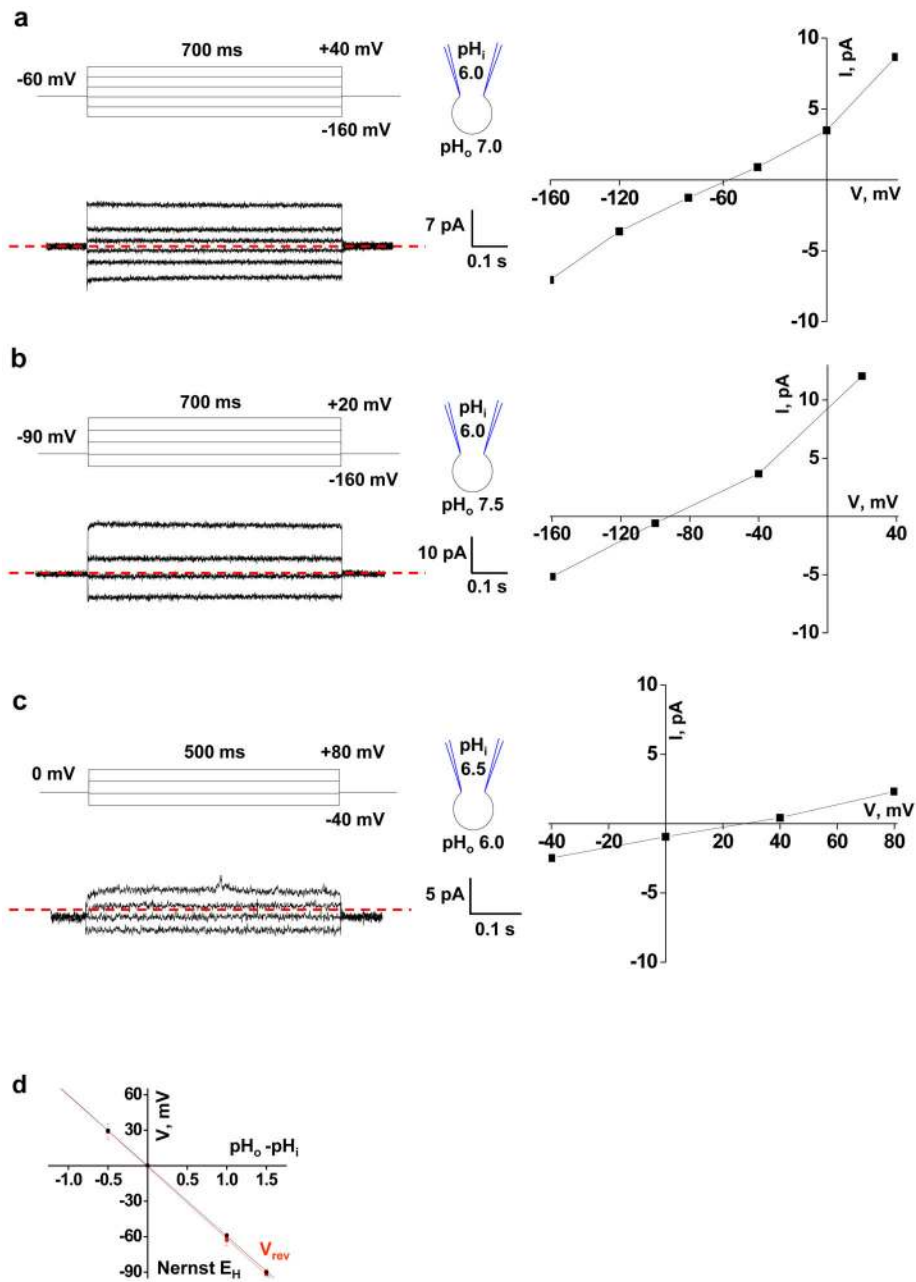
**Extended Data Figure 3 |. H$^+$ selectivity of mitochondrial $I_H$.**

**a**, *Left panel*, representative mitochondrial $I_H$ recorded at $\Delta$pH = 1 in response to the voltage step protocol indicated at the top (SM mitoplast, n=6); $\Delta V$ = 40 mV. A holding potential of −60 mV (close to the $E_H$) was selected to minimize H$^+$ current and depletion of the proton buffer between applications of voltage steps. A zero current level is indicated by the red dotted line. *Right panel,* the I/V curve corresponding to the current traces in the left panel (SM mitoplast, n=6). Note the reversal potential. The pH values in the pipette and bath solutions are indicated on the diagram. **b**, *Left panel,* mitochondrial $I_H$ recorded at $\Delta$pH = 1.5 in response to the voltage step protocol indicated at the top of the panel (SM mitoplast, n=3); $\Delta V$ = 60 mV. Holding potential was −90 mV (close to the $E_H$). *Right panel,* the I/V

curve corresponding to the current traces in the left panel (SM mitoplast, n=6). **c,** *Left panel,* mitochondrial $I_H$ recorded at $\Delta pH = -0.5$ in response to the voltage step protocol indicated at the top of the panel (SM mitoplast, n=4); $\Delta V = 40$ mV. Holding potential was 0 mV. *Right panel,* the I/V curve corresponding to the current traces in the left panel. All currents were induced by 1.5 μM AA (SM mitoplast, n=6). **d,** $I_H$ reversal potentials ($V_{rev}$) compared to Nernst $H^+$ equilibrium potentials ($E_H$). Linear fitting of $V_{rev}$ (red) and $E_H$ at 24°C (black) vs. transmembrane $\Delta pH$; pH 6/7, n=6; pH 6/7.5, n=3; pH 6.5/6, n=4. SM mitoplasts. Data represent mean±SEM.
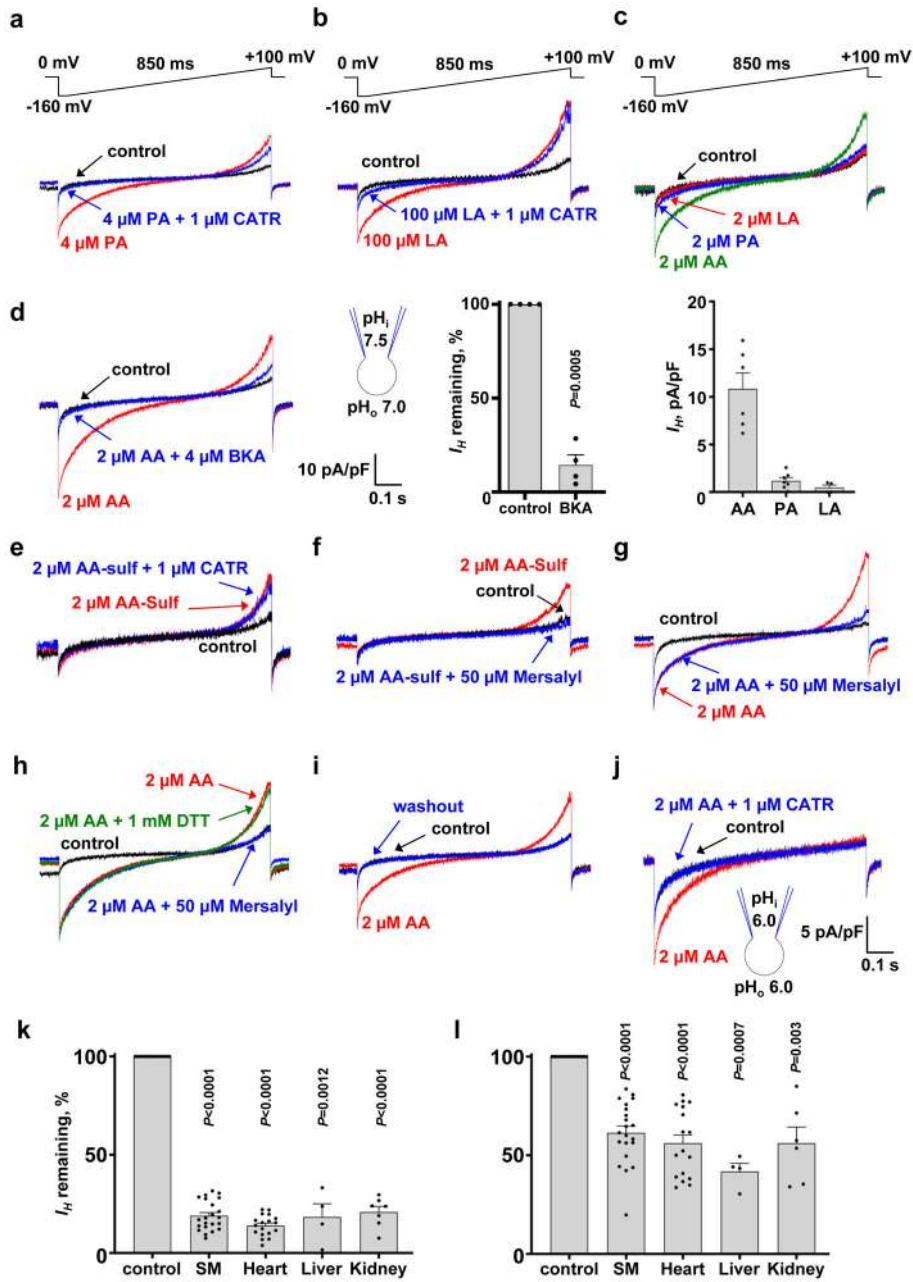
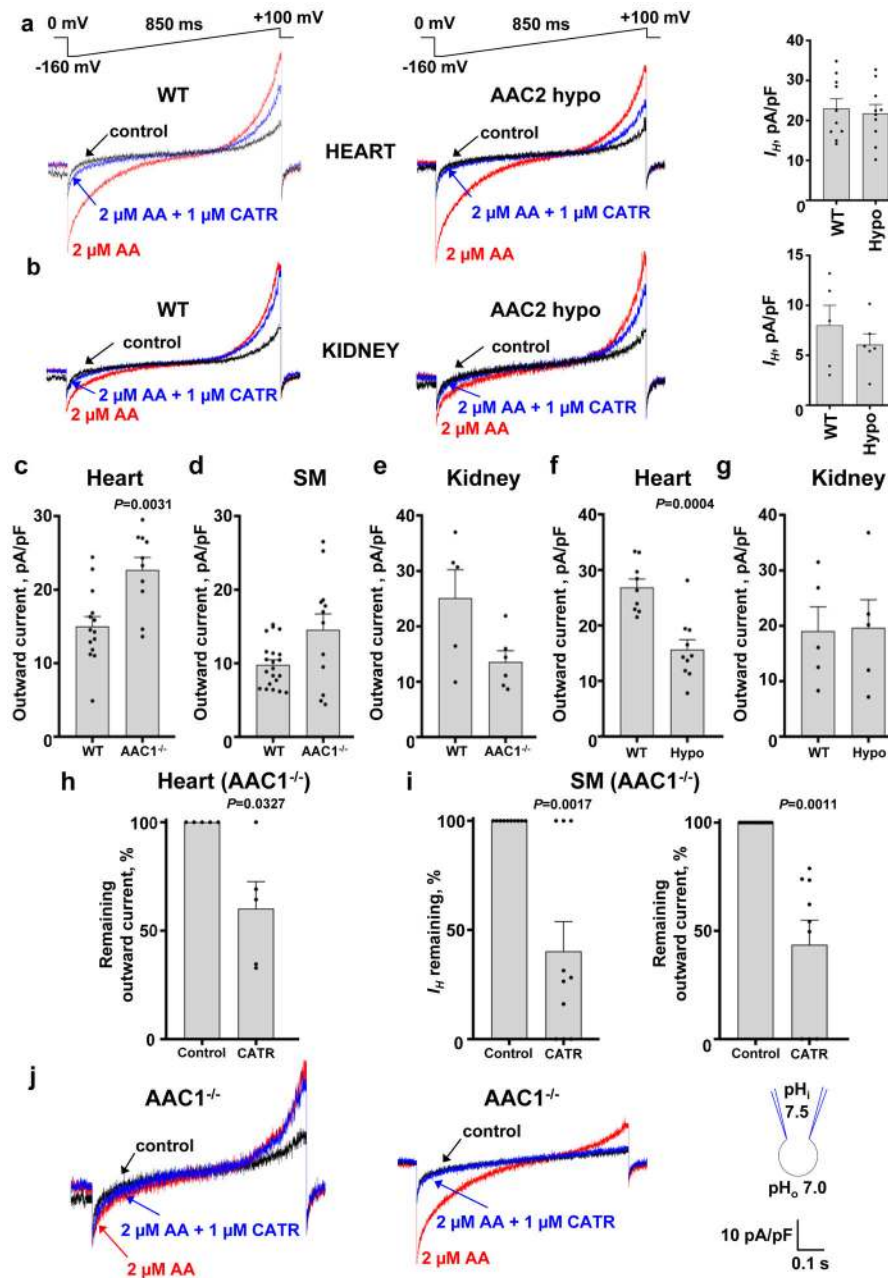**Extended Data Figure 4 |. AAC-dependent and -independent currents induced by FA.**
**a**, Current induced by 4 μM palmitic acid (PA, red) was inhibited by 1 μM CATR (blue).
Control current is shown in black. Representative experiments performed in heart mitoplasts,
n=4. **b**, The same experiment performed with 100 μM lauric acid (LA), n=5. **c**, *Upper panel,*
currents induced by 2 2 μM of AA (green), PA (blue), and LA (red) in the same mitoplast.
Control current is shown in black. Heart mitoplasts, n=4. *Lower panel,* mean $I_H$ current
densities at −160 mV induced by 2 μM of AA (n=6), PA (n=7), and LA (n=4) as in
experiment shown in the upper panel. Heart mitoplasts. Data represent mean±SEM. **d**, *Left
panel:* $I_H$ induced by 2 μM AA (red) was inhibited by 4 μM BKA (blue). Control currents
are shown in black. Representative experiment performed in a heart mitoplast (n=4). *Right*

*panel:* inhibition of $I_H$ induced by 2 μM AA in heart mitoplasts by 4 μM BKA. Remaining $I_H$ measured at −160 mV is shown as a percentage of control, n=4. Paired t-test, two-tailed. Data represent mean±SEM. **e**, Current induced by 2 μM AA sulfonate before (red) and after (blue) addition of 1 μM CATR. Representative experiment performed in heart mitoplast. n=6. **f**, Current induced by 2 μM AA sulfonate before (red) and after (blue) addition of 50 μM mersalyl. Representative experiment performed in a heart mitoplast. n=4. **g**, Currents induced by 2 μM AA before (red) and after (blue) addition of 50 μM mersalyl. Note that only the outward current was inhibited. Representative experiment performed in a heart mitoplast. n=6. **h**, The outward current activated by 2 μM AA (red) is inhibited by 50 μM mersalyl (blue) and is next recovered by 1 mM DTT (green). Control current is shown in black. Heart mitoplasts, n= 4. **i,** Whole-mitoplast current before (control, black), after application of 2 μM AA (red), and upon washout of AA (blue). Heart mitoplasts, n=6. **j**, $I_H$ induced by 2 μM AA (red) was inhibited by 1 μM CATR (blue). Control current is shown in black. Symmetrical pH 6.0. Heart mitoplasts, n=4. **k**, Inhibition of the inward $I_H$ induced by 2 μM AA in SM, heart, liver, and kidney by 1 μM CATR. SM (n=22), heart (n=18), liver (n=4), and kidney (n=7) for both control and CATR treatment. Remaining inward current measured at −160 mV is shown as a percentage of control. Paired t test, two-tailed. Data represent mean±SEM. **l**, Inhibition of the outward current induced by 2 μM AA in SM, heart, liver, and kidney by 1 μM CATR. Remaining outward current measured at +100 mV is shown as a percentage of control. SM (n=21), heart (n=17), liver (n=4), and kidney (n=7) for both control and CATR treatment. Paired t-test, two-tailed. Data represent mean±SEM.
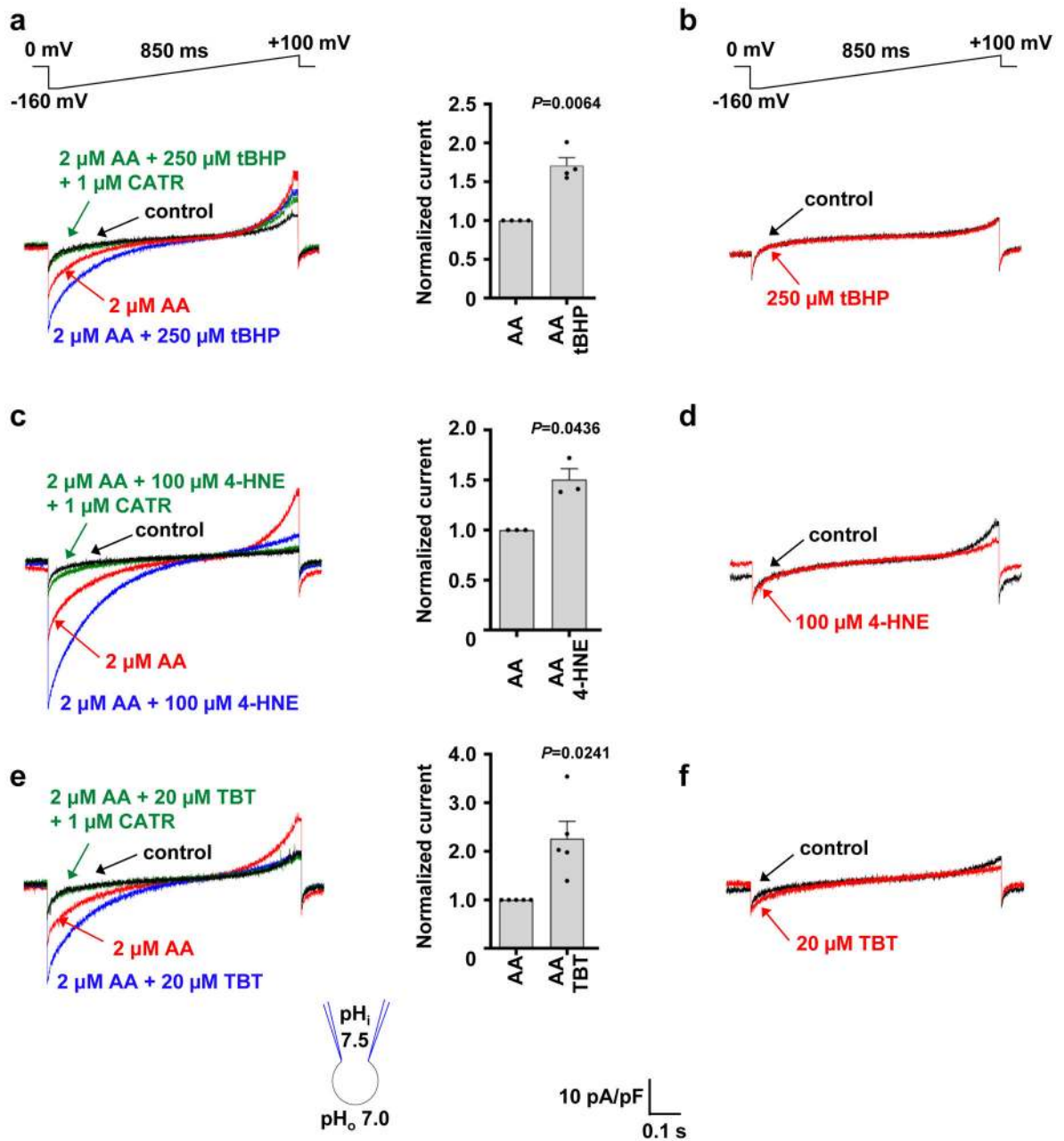
**Extended Data Figure 5 |. FA-dependent $I_H$ via AAC is potentiated by oxidation.**
**a,c,e,** $I_H$ activated by 2 μM AA (red) was then potentiated by oxidizers 250 μM tBHP, 100 μM 4-HNE, or 20 μM TBT (blue). $I_H$ potentiated by oxidizers was inhibited by CATR (green). Control current is shown in black. Bar graphs show ratio of $I_H$ amplitudes at −160 mV before and after addition of oxidizer. Heart mitoplasts. Note that TBT and 4-HNE, but not tBHP, inhibited the AAC-independent outward current observed at positive membrane potentials. Panel (a) n=4, panel (c) n=3, and panel (e) n=5 for all experimental conditions. Paired t-test, two-tailed. Data represent mean±SEM. **b,d,f,** Currents before (control, black) and after (red) application of 250 μM tBHP (n=3), 20 μM TBT (n=3), and 100 μM 4-HNE (n=3).

**Extended Data Figure 6 |. FA-dependent currents in *AAC1* knockout and *AAC2* hypomorphic mice.**
**a and b**, Representative currents induced by 2 μM AA in WT and *AAC2* hypomorphic mitoplasts of heart (n=9 for WT and n=9 for hypo) (a) and kidney (n=4 for WT and n=5 for hypo) (b). *Right panels:* $I_H$ current densities at −160 mV for WT (n=10 for heart and n=5 for kidney) and *AAC2* hypomorphic mitoplasts (n=10 for heart and n=6 for kidney). Data are mean±SEM. **c-e**, Densities of the outward current measured at +100 mV for WT and *AAC1*^{−/−} mitoplasts of heart (n=14 for WT and n=10 for *AAC1*^{−/−}), SM (n=21 for WT and n=12 for *AAC1*^{−/−}), and kidney (n=5 for WT and n=6 for *AAC1*^{−/−}). Mann-Whitney test, two-tailed. Data are mean±SEM. **f and g**, Densities of the outward current measured at +100

mV for WT (n=9 for heart and n=5 for kidney) and *AAC2* hypomorphic (n=10 for heart and n=5 for kidney) mitoplasts of heart and kidney. Mann-Whitney test, two-tailed. Data are mean±SEM. **h**, Inhibition of the outward current induced by 2 μM AA in *AAC1*$^{-/-}$ heart mitoplasts by 1 μM CATR (n=5, control and CATR). Remaining outward current measured at +100 mV is shown as a percentage of control. Paired t-test, two-tailed. Data are mean ±SEM. **i**, *Left panel:* inhibition of inward $I_H$ induced by 2 μM AA in *AAC1*$^{-/-}$ SM mitoplasts by 1 μM CATR (n=10, control and CATR). Remaining $I_H$ measured at −160 mV is shown as a percentage of control. *Right panel:* inhibition of the outward current induced by 2 μM AA in in *AAC1*$^{-/-}$ SM mitoplasts by 1 μM CATR (n=9, control and CATR). Remaining current measured at +100 mV is shown as a percentage of control. Paired t-test, two-tailed. Data are mean±SEM. **j**, Two representative experiments in which the $I_H$ induced by 2μM AA in *AAC1*$^{-/-}$ mitoplasts of SM was the smallest (left panel, n=4) and the largest (right panel, n=3). $I_H$ induced by 2 μM AA (red) was inhibited by 1 μM CATR (blue). Control current is shown in black.
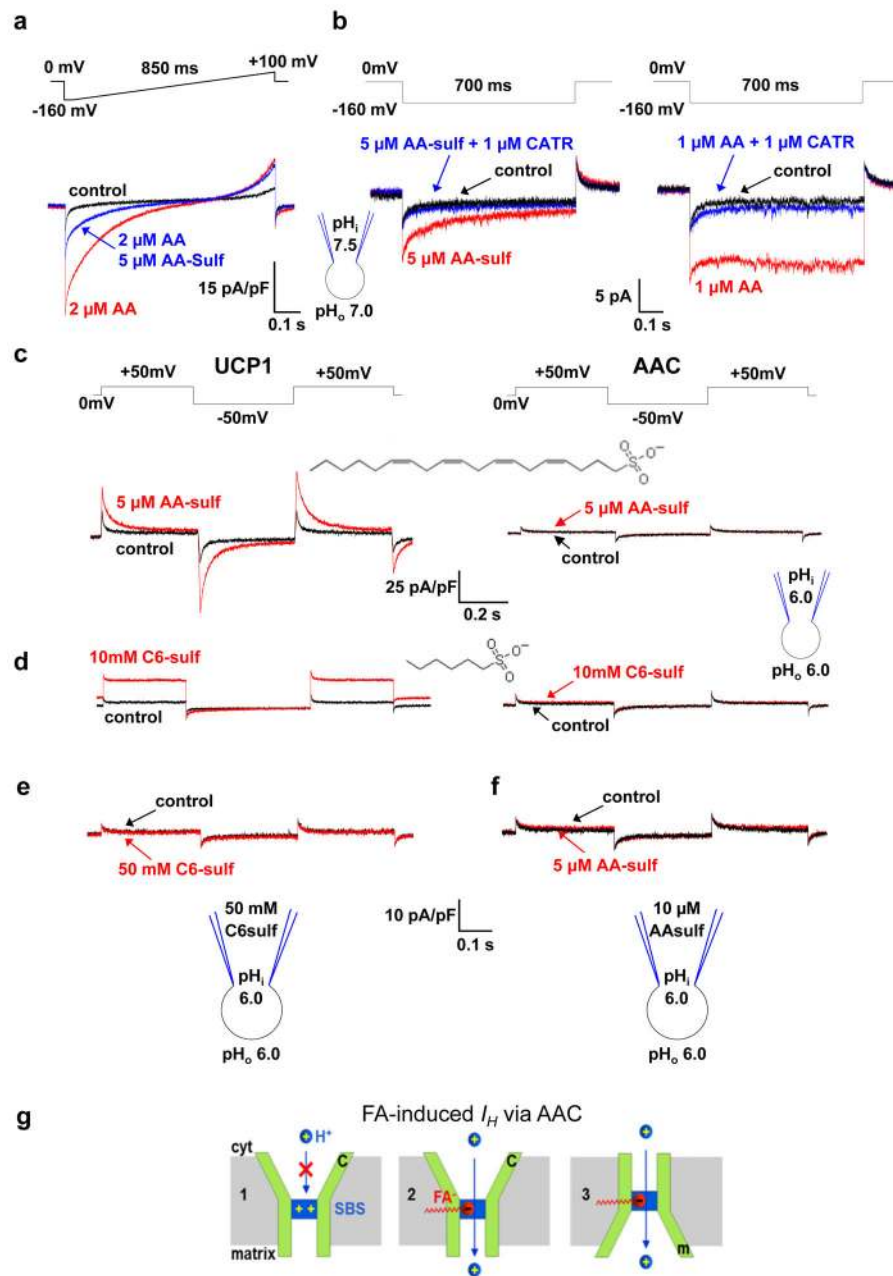
**Extended Data Figure 7 |. Interaction of FA anions with AAC.**

**a**, $I_H$ induced by 2 μM AA (red) was inhibited by 66±2% (n=4, SM mitoplasts) by 5 μM AA-sulf (blue). Data are mean±SEM. **b**, Current induced by 5 μM AA-sulf (left panel, red) or 1 μM AA (right panel, red) was inhibited by 1 μM CATR (blue). Control currents are shown in black. Smaller [AA] was used to induce comparable currents with AA-sulf. Heart mitoplasts, n=4. **c** and **d**, Currents recorded before (control, black) and after addition of 5 μM AA-sulf (c) or 10 mM C6-sulf (d) to bath (red). Brown fat mitoplast (UCP1, left panel), heart mitoplast (AAC, right panel), n=4 for each. Currents were measured at pH 6.0 to inhibit the production of FA by phospholipase A2 (PLA2) associated with the brown fat IMM and ensure that UCP1 currents were activated by exogenously applied FA anions only.

**e**, Current before (control, black) and after (red) application of 50 mM C6-sulf to the bath. Pipette solution contained 50 mM C6-sulf. Symmetrical pH 6.0. Heart mitoplasts, n=3. **f**, Current before (control, black) and after (red) application of 5 μM AA-sulf to the bath. Pipette solution contained 10 μM AA-sulf. Bath AA-sulf was kept at 5 μM because higher concentrations disrupted the IMM. Symmetrical pH 6.0. Heart mitoplasts, n=3. **g**, Proposed model of FA-dependent $I_H$ via AAC. Without FA, AAC is impermeable for $H^+$ (1). When FA binds in the AAC translocation pathway, its protonatable headgroup enables $H^+$ binding and transport (2). FA can activate $I_H$ with AAC in either the c- or m-state (2 and 3). Because the SBS is positively charged and retains its structure with c–m conformational change, the negatively charged head of FA is likely to interact with the SBS, while the hydrophobic carbon tail may protrude into the membrane and/or be stabilized by hydrophobic interactions within AAC (2 and 3).
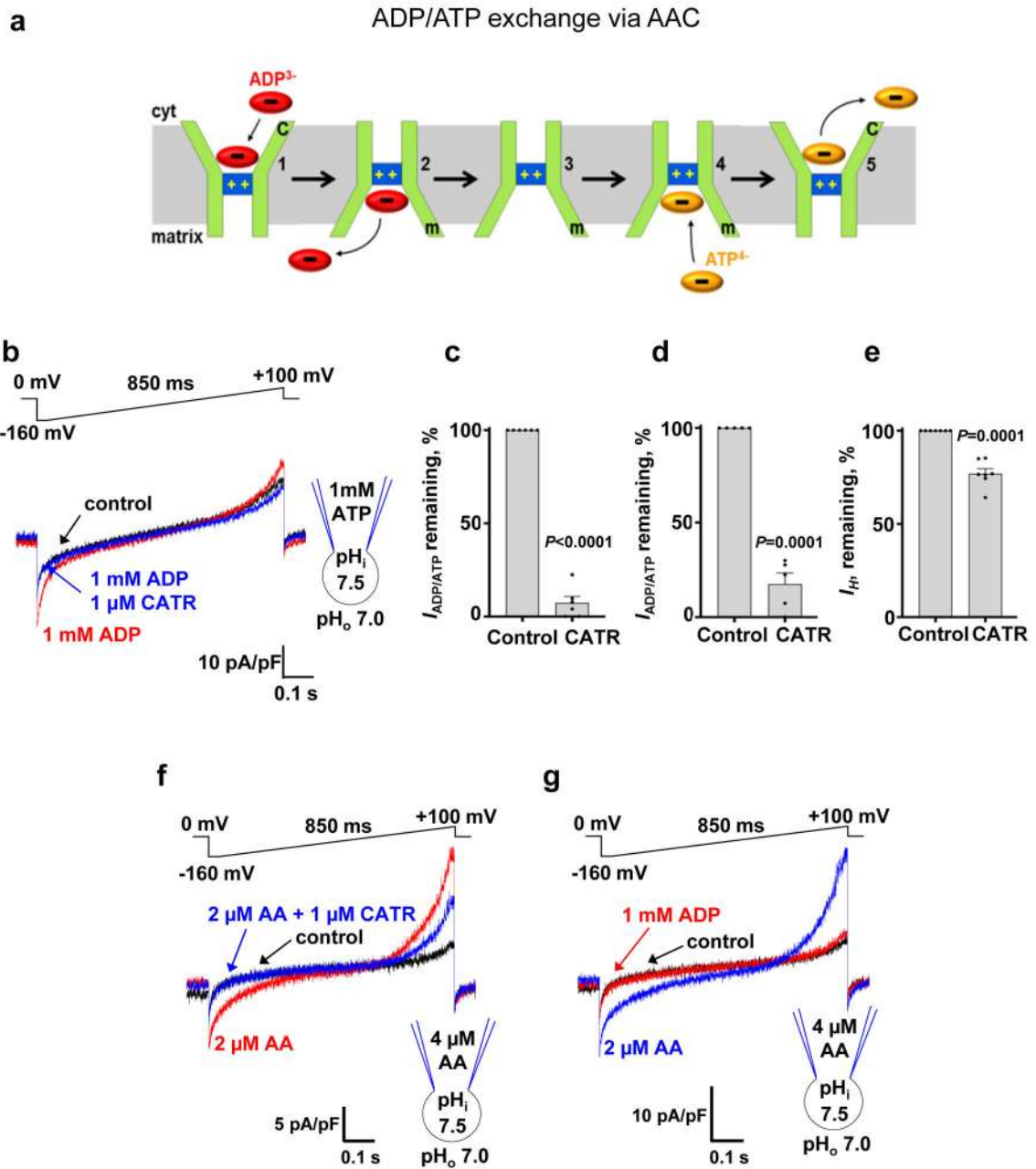
**Extended Data Figure 8 |. Adenine nucleotide exchange by AAC.**

**a**, The alternating access mechanism of adenine nucleotide transport by AAC. AAC is shown in green, and its substrate-binding site (SBS, overall positively charged) located in the middle of the membrane is shown in blue. Cytosolic ADP binds to AAC in the c-state (1). AAC transitions to the m-state, and ADP is released into the matrix (2 and 3). Matrix ATP binds to AAC in the m-state (4). AAC transitions to the c-state, and ATP is released into the cytosol (5). **b**, AAC current activated by 1 mM ADP (red) is inhibited by 1μM CATR (blue). Pipette solution contained and 1 mM ATP. Heart mitoplast, n=3. Control trace is in black. **c**, Inhibition of the inward ADP/ATP exchange current via AAC by 1 μM CATR. Heart mitoplast, n=6 (control and CATR treatment). Paired t-test, two-tailed. Data are mean±SEM.

Remaining inward current measured at −160 mV is shown as a percentage of control. See also Fig. 3a. **d**, Inhibition of the outward ATP/ADP exchange current via AAC by 1 μM CATR. Heart mitoplast, n=5 (control and CATR treatment). Paired t-test, two-tailed. Data are mean±SEM. Remaining outward current measured at −100 mV is shown as a percentage of control. See also Fig. 3b. **e**, Inhibition of the inward $I_H$ induced by 2 μM AA by 1 μM CATR after ADP pre-treatment. Heart mitoplast, n=7 (control and CATR treatment). Paired t-test, two-tailed. Data are mean±SEM. Remaining $I_H$ measured at −160 mV is shown as a percentage of control. See also Fig. 3e. **f**, Current before (control, black) and after (red) addition of 2 μM AA to bath. Subsequent addition of 1 μM CATR (blue) inhibited $I_H$. Pipette solution contained 4 μM AA. Heart mitoplast, n=4. **g**, Control current (black) and current after addition of 1 mM ADP to the bath solution (red). AA (2 μM) was added to the bath solution at the end of experiment (blue). Pipette solution contained 4 μM AA. Heart mitoplasts, n=4.
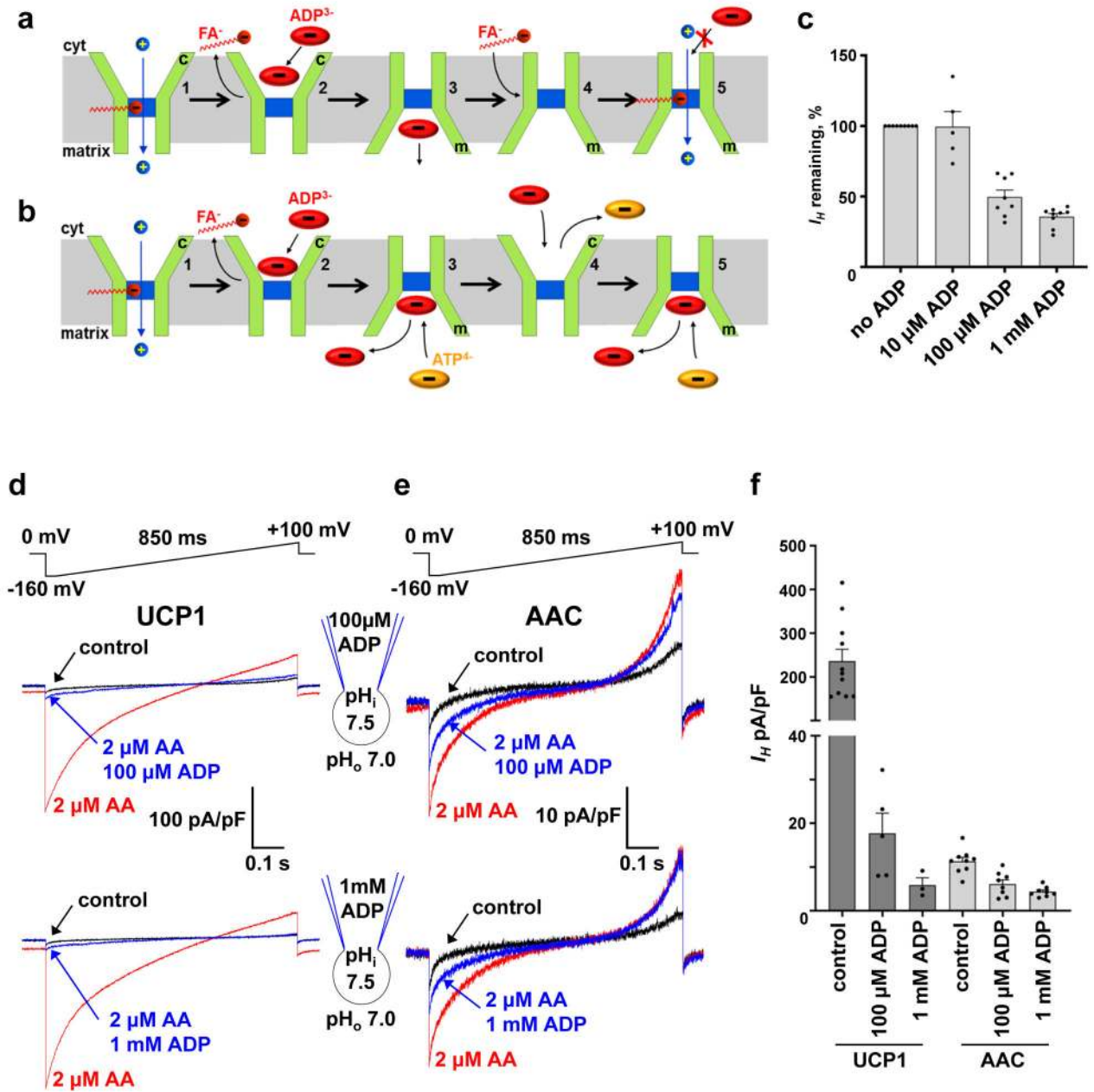
**Extended Data Figure 9 |. Regulation of FA-dependent $I_H$ by nucleotides.**
**a**, Explanation of transient $I_H$ inhibition by cytosolic adenine nucleotides. AAC in c-state, with FA anion in the translocation pathway, mediates $I_H$ (1). Cytosolic $ADP^{3-}$ binds in c-state and expels FA anion/blocks translocation pathway, leading to $I_H$ inhibition (2). Upon AAC conformation change, ADP dissociates into matrix (pipette) solution (3). FA anion re-associates with AAC in m-state, restoring $I_H$ (4). Cytosolic ADP cannot inhibit $I_H$ while AAC is in m-state (5). See also Fig. 4a. **b**, Proposed mechanism of $I_H$ inhibition by adenine nucleotide exchange. AAC in c-state, with FA anion in the translocation pathway, mediates $I_H$ (1). Cytosolic $ADP^{3-}$ binds in c-state and expels FA anion/blocks translocation pathway, leading to $I_H$ inhibition (2). The resultant continuous exchange of cytosolic and matrix

adenine nucleotides inhibits FA anion binding and $I_H$ (3, 4, and 5). ATP (and not ADP) is shown as a matrix adenine nucleotide to reflect physiological conditions. See also Fig. 4b. **c,** Remaining $I_H$ after inhibition by different concentrations of ADP applied to both sides of the IMM to induce continuous adenine nucleotide exchange via AAC as in (e). ADP/ADP exchange was used to avoid contaminating $I_H$ with ADP/ATP exchange current. Heart and SM mitoplasts, n=5 (control and 10 μM ADP), n=8 (control and 100 μM ADP, n=9 (control and 1 mM ADP). Data are mean±SEM. **d,** $I_H$ via UCP1 is inhibited by 100 μM $Mg^{2+}$-free ADP (upper panel, n=5) and 1 mM $Mg^{2+}$-free ADP (lower panel, n=3). $I_H$ activated by 2 μM AA is shown before (red) and after inhibition by ADP (blue). In the beginning of the experiment, before the application of AA, the endogenous membrane FA were removed by a 30-40s pre-treatment with 10 mM MβCD (black, control). All recording solutions contained 1 μM CATR to reduce AAC contribution to the $I_H$ measured. Pipette solution contained either 100 μM ADP (upper panel) or 1 mM ADP (lower panel) to match the recording conditions for AAC (e). Brown fat mitoplasts. **e,** $I_H$ via AAC is inhibited by 100 μM $Mg^{2+}$-free ADP (upper panel, n=8) and 1 mM $Mg^{2+}$-free ADP (lower panel, n=8). $I_H$ activated by 2 μM AA is shown before (red) and after inhibition by ADP (blue). Pipette solution contained either 100 μM ADP (upper panel) or 1 mM ADP (lower panel) to achieve symmetrical [ADP] on both side of IMM. Heart mitoplasts. **f,** Mean densities of $I_H$ via UCP1 (dark grey) and AAC (light grey) in control (brown fat, n=11 and heart, n=9) and in the presence of 100 μM (brown fat, n=5 and heart, n=8) and 1 mM ADP (brown fat, n=3 and heart, n=8) on both sides of the IMM. $I_H$ amplitudes were measured at −160 mV. The same data as in Fig. 4e. Data represent mean±SEM.
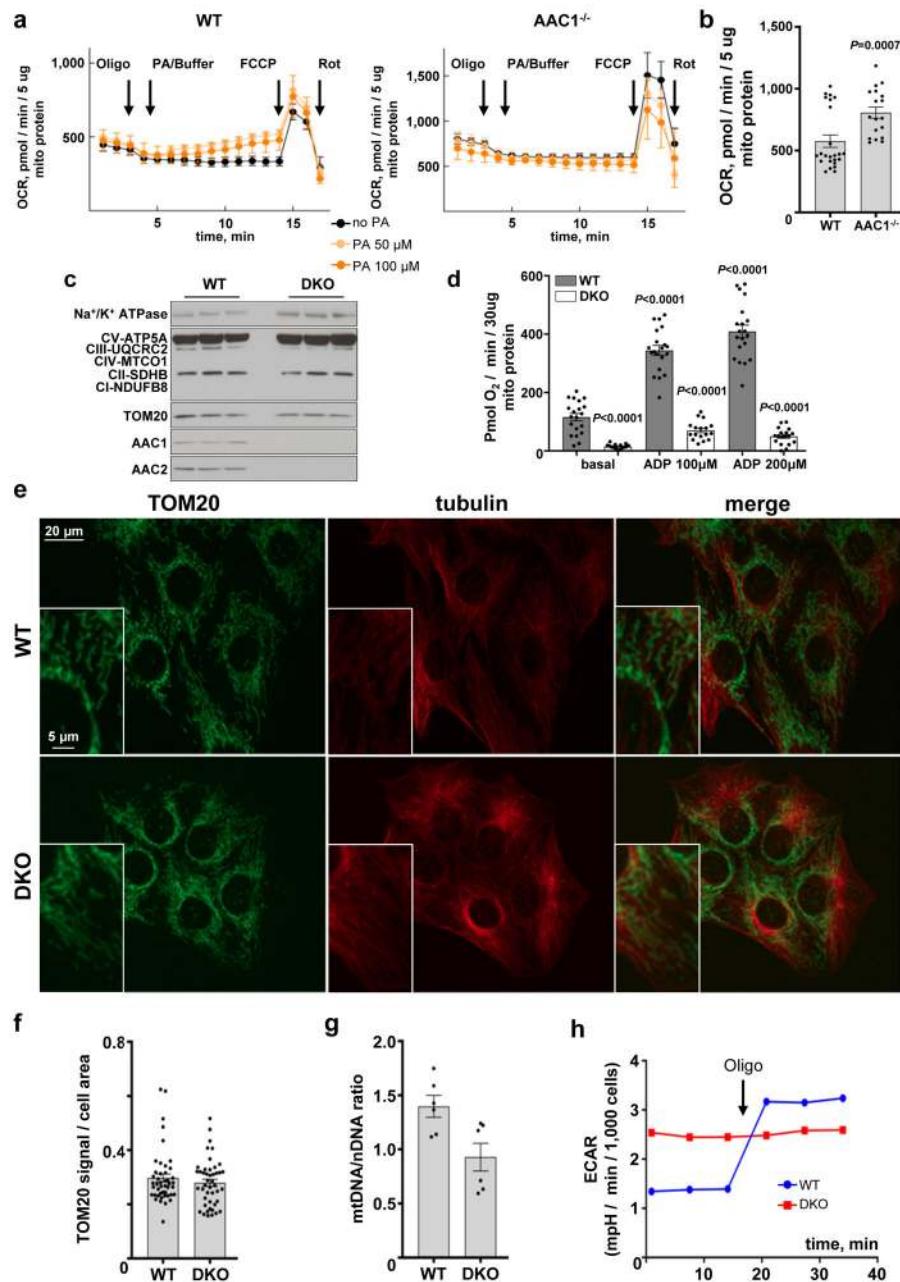
**Extended Data Figure 10 |. Phenotypes associated with AAC deficiency.**
**a,** Representative OCRs of isolated heart mitochondria from WT (left panel, n=3 wells) and *AAC1⁻/⁻* mice (right panel, n=4 wells). As indicated by the arrows, first oligomycin and then either palmitic acid (PA: 50 μM, light orange and 100 μM, dark orange) or buffer (black) were added, following by FCCP and rotenone. Higher PA concentrations were used than those for electrophysiological experiments, because in suspensions of isolated mitochondria and in the presence of albumin, the effective concentration of PA is significantly lower. FCCP-induced uncoupled respiration in WT and *AAC1⁻/⁻* mitochondria validated their respiration capacity. Data represent mean±SEM. This experiment was repeated with independent mitochondrial isolations in WT (n=4) and *AAC*1⁻/⁻ (n=3) with

the same results. **b**, Basal OCR of isolated heart mitochondria of WT (n=24 wells) and *AAC1*$^{-/-}$ (n= 18 wells) mice. Mann-Whitney test, two-tailed. Data represent mean±SEM. **c**, Representative immunoblots in WT (n=5) and DKO (n=7) C2C12 cells for: NDUFB8 (complex I, CI), SDHA (complex II, CII), core 2 subunit (complex III, CIII), CIV-I subunit (complex IV, CIV), and ATP5A (complex V, CV), TOM20, and the loading control (plasma membrane Na$^+$/K$^+$ ATPase). For gel source data see Supplementary Figure 1. **d**, Basal and ADP-stimulated OCR of mitochondria from WT (basal, ADP 100 μM, and ADP 200 μM, n=20) and DKO (n=16 for basal, n=16 for ADP 100 μM, and n=17 for ADP 200 μM) C2C12 cells. Mann-Whitney test, two-tailed. Data represent mean±SEM. **e**, Representative confocal micrographs of WT (upper panels, n=45 cells) and DKO (lower panels, n=45 cells) C2C12 cells immunolabeled with TOM20 (green) and tubulin (red) antibodies. Insets show magnified area from the same images. **f**, Mitochondrial biomass per cell in WT and DKO C2C12 cells, calculated as a ratio between TOM20 signal and the total area of the cell, n=45 per each group. Data represent mean±SEM. **g,** Comparison of a ratio between mitochondrial DNA (mtDNA) and nuclear DNA (nDNA) from WT (n=6) and DKO (n=6) C2C12 cells. Data represent mean±SEM. **h,** Kinetic study of ECAR in WT (n=22) and DKO (n=22) C2C12 cells under basal conditions and upon addition of oligomycin into the respiration medium. Note that inhibition of mitochondrial ATP production in DKO cells with oligomycin did not affect ECAR, whereas in WT cells, oligomycin potently stimulated ECAR. Data represent mean±SEM.

## Supplementary Material

Refer to Web version on PubMed Central for supplementary material.

## ACKNOWLEDGMENTS

## REFERENCES

1. Klingenberg M The ADP and ATP transport in mitochondria and its carrier. Biochim Biophys Acta 1778, 1978–2021, doi:S0005-2736(08)00144-2 [pii]10.1016/j.bbamem.2008.04.011 (2008). [PubMed: 18510943]

2. Stepien G, Torroni A, Chung AB, Hodge JA & Wallace DC Differential expression of adenine nucleotide translocator isoforms in mammalian tissues and during muscle cell differentiation. J Biol Chem 267, 14592–14597 (1992). [PubMed: 1378836]

3. Rodic N et al. DNA methylation is required for silencing of ant4, an adenine nucleotide translocase selectively expressed in mouse embryonic stem cells and germ cells. Stem Cells 23, 1314–1323, doi:10.1634/stemcells.2005-0119 (2005). [PubMed: 16051982]

4. Levy SE, Chen YS, Graham BH & Wallace DC Expression and sequence analysis of the mouse adenine nucleotide translocase 1 and 2 genes. Gene 254, 57–66 (2000). [PubMed: 10974536]

5. Graham BH et al. A mouse model for mitochondrial myopathy and cardiomyopathy resulting from a deficiency in the heart/muscle isoform of the adenine nucleotide translocator. Nat Genet 16, 226–234, doi:10.1038/ng0797-226 (1997). [PubMed: 9207786]

6. Ruprecht JJ et al. The Molecular Mechanism of Transport by the Mitochondrial ADP/ATP Carrier. Cell, doi:10.1016/j.cell.2018.11.025 (2019).

7. Andreyev A et al. Carboxyatractylate inhibits the uncoupling effect of free fatty acids. FEBS lett 226, 265–269 (1988). [PubMed: 3338558]

8. Skulachev VP Uncoupling: new approaches to an old problem of bioenergetics. Biochim Biophys Acta - Bioenergetics 1363, 100–124, doi:10.1016/s0005-2728(97)00091-1 (1998).

9. Brustovetsky N & Klingenberg M The reconstituted ADP/ATP carrier can mediate H+ transport by free fatty acids, which is further stimulated by mersalyl. J Biol Chem 269, 27329–27336 (1994). [PubMed: 7961643]

10. Brand MD et al. The basal proton conductance of mitochondria depends on adenine nucleotide translocase content. Biochem J 392, 353–362, doi:BJ20050890 [pii]10.1042/BJ20050890 (2005). [PubMed: 16076285]

11. Halestrap AP & Richardson AP The mitochondrial permeability transition: A current perspective on its identity and role in ischaemia/reperfusion injury. J Mol Cell Cardiol, doi:10.1016/j.yjmcc. 2014.08.018 (2014).

12. Bernardi P, Rasola A, Forte M & Lippe G The Mitochondrial Permeability Transition Pore: Channel Formation by F-ATP Synthase, Integration in Signal Transduction, and Role in Pathophysiology. Physiol Rev 95, 1111–1155, doi:10.1152/physrev.00001.2015 (2015). [PubMed: 26269524]

13. Korshunov SS, Skulachev VP & Starkov AA High protonic potential actuates a mechanism of production of reactive oxygen species in mitochondria. FEBS lett 416, 15–18 (1997). [PubMed: 9369223]

14. Wojtczak L & Schonfeld P Effect of fatty acids on energy coupling processes in mitochondria. Biochim Biophys Acta 1183, 41–57 (1993). [PubMed: 8399375]

15. Bouillaud F, Weissenbach J & Ricquier D Complete cDNA-derived amino acid sequence of rat brown fat uncoupling protein. J Biol Chem 261, 1487–1490 (1986). [PubMed: 3753702]

16. Aquila H, Link TA & Klingenberg M The uncoupling protein from brown fat mitochondria is related to the mitochondrial ADP/ATP carrier. Analysis of sequence homologies and of folding of the protein in the membrane. EMBO J 4, 2369–2376 (1985). [PubMed: 3000775]

17. Fedorenko A, Lishko PV & Kirichok Y Mechanism of Fatty-Acid-Dependent UCP1 Uncoupling in Brown Fat Mitochondria. Cell 151, 400–413, doi:10.1016/j.cell.2012.09.010 S0092-8674(12)01113-0 [pii] (2012). [PubMed: 23063128]

18. Bertholet AM et al. Mitochondrial Patch Clamp of Beige Adipocytes Reveals UCP1-Positive and UCP1-Negative Cells Both Exhibiting Futile Creatine Cycling. Cell Metab 25, 811–822 e814, doi: 10.1016/j.cmet.2017.03.002 (2017). [PubMed: 28380374]

19. Roussel D, Harding M, Runswick MJ, Walker JE & Brand MD Does any yeast mitochondrial carrier have a native uncoupling protein function? J Bioenerg Biomembr 34, 165–176 (2002). [PubMed: 12171066]

20. Echtay KS, Winkler E, Frischmuth K & Klingenberg M Uncoupling proteins 2 and 3 are highly active H$^+$ transporters and highly nucleotide sensitive when activated by coenzyme Q (ubiquinone). Proc Natl Acad Sci U S A 98, 1416–1421, doi:10.1073/pnas.98.4.1416 (2001). [PubMed: 11171965]

21. Jaburek M et al. Transport function and regulation of mitochondrial uncoupling proteins 2 and 3. J Biol Chem 274, 26003–26007 (1999). [PubMed: 10473545]

22. Krauss S, Zhang CY & Lowell BB The mitochondrial uncoupling-protein homologues. Nat Rev Mol Cell Biol 6, 248–261 (2005). [PubMed: 15738989]

23. Samartsev VN et al. Involvement of aspartate/glutamate antiporter in fatty acid-induced uncoupling of liver mitochondria. Biochim Biophys Acta - Bioenergetics 1319, 251–257, doi:10.1016/s0005-2728(96)00166-1 (1997).

24. Wieckowski MR & Wojtczak L Involvement of the dicarboxylate carrier in the protonophoric action of long-chain fatty acids in mitochondria. Biochim Biophys Res Commun 232, 414–417, doi:S0006291X97962987 [pii] (1997). [PubMed: 9125192]

25. Zackova M, Kramer R & Jezek P Interaction of mitochondrial phosphate carrier with fatty acids and hydrophobic phosphate analogs. Int J Biochem Cell Biol 32, 499–508 (2000). [PubMed: 10736565]

26. Engstova H et al. Natural and azido fatty acids inhibit phosphate transport and activate fatty acid anion uniport mediated by the mitochondrial phosphate carrier. J Biol Chem 276, 4683–4691, doi: 10.1074/jbc.M009409200 (2001). [PubMed: 11085992]

27. Gutknecht J Proton conductance caused by long-chain fatty acids in phospholipid bilayer membranes. J Membr Biol 106, 83–93 (1988). [PubMed: 2852256]

28. Kokoszka JE et al. The ADP/ATP translocator is not essential for the mitochondrial permeability transition pore. Nature 427, 461–465 (2004). [PubMed: 14749836]

29. Penzo D, Tagliapietra C, Colonna R, Petronilli V & Bernardi P Effects of fatty acids on mitochondria: implications for cell death. Biochim Biophys Acta - Bioenergetics 1555, 160–165, doi:10.1016/S0005-2728(02)00272-4 (2002).

30. Wieckowski MR & Wojtczak L Fatty acid-induced uncoupling of oxidative phosphorylation is partly due to opening of the mitochondrial permeability transition pore. FEBS lett 423, 339–342 (1998). [PubMed: 9515735]

31. Schonfeld P & Bohnensack R Fatty acid-promoted mitochondrial permeability transition by membrane depolarization and binding to the ADP/ATP carrier. FEBS lett 420, 167–170 (1997). [PubMed: 9459303]

32. Nedergaard J & Cannon B The 'novel' 'uncoupling' proteins UCP2 and UCP3: what do they really do? Pros and cons for suggested functions. Exp Physiol 88, 65–84, doi:EPH_8802502 [pii] (2003). [PubMed: 12525856]

33. Bouillaud F UCP2, not a physiologically relevant uncoupler but a glucose sparing switch impacting ROS production and glucose sensing. Biochim Biophys Acta 1787, 377–383, doi:S0005-2728(09)00010-3 [pii]10.1016/j.bbabio.2009.01.003 (2009). [PubMed: 19413946]

34. Vozza A et al. UCP2 transports C4 metabolites out of mitochondria, regulating glucose and glutamine oxidation. Proc Natl Acad Sci U S A 111, 960–965, doi:10.1073/pnas.1317400111 (2014). [PubMed: 24395786]

35. Echtay KS et al. Superoxide activates mitochondrial uncoupling proteins. Nature 415, 96–99, doi: 10.1038/415096a415096a [pii] (2002). [PubMed: 11780125]

36. Echtay KS et al. A signalling role for 4-hydroxy-2-nonenal in regulation of mitochondrial uncoupling. EMBO J 22, 4103–4110, doi:10.1093/emboj/cdg412 (2003). [PubMed: 12912909]

37. Parker N, Affourtit C, Vidal-Puig A & Brand MD Energization-dependent endogenous activation of proton conductance in skeletal muscle mitochondria. Biochem J 412, 131–139, doi:BJ20080006 [pii]10.1042/BJ20080006 (2008). [PubMed: 18251717]

38. Nishikimi A et al. Tributyltin interacts with mitochondria and induces cytochrome c release. Biochem J 356, 621–626 (2001). [PubMed: 11368793]

39. Vieira HL et al. The adenine nucleotide translocator: a target of nitric oxide, peroxynitrite, and 4-hydroxynonenal. Oncogene 20, 4305–4316 (2001). [PubMed: 11466611]

40. Cunningham SA, Wiesinger H & Nicholls DG Quantification of fatty acid activation of the uncoupling protein in brown adipocytes and mitochondria from the guinea-pig. Eur J Biochem 157, 415–420 (1986). [PubMed: 3709541]

41. Klingenberg M & Huang SG Structure and function of the uncoupling protein from brown adipose tissue. Biochim Biophys Acta 1415, 271–296 (1999). [PubMed: 9889383]

42. Cho J et al. Mitochondrial ATP transporter Ant2 depletion impairs erythropoiesis and B lymphopoiesis. Cell Death Differ 22, 1437–1450, doi:10.1038/cdd.2014.230 (2015). [PubMed: 25613378]

43. Morrow RM et al. Mitochondrial energy deficiency leads to hyperproliferation of skeletal muscle mitochondria and enhanced insulin sensitivity. Proc Natl Acad Sci U S A 114, 2705–2710, doi: 10.1073/pnas.1700997114 (2017). [PubMed: 28223503]

44. Bertholet AM & Kirichok Y UCP1: A transporter for $H^+$ and fatty acid anions. Biochimie 134, 28–34, doi:10.1016/j.biochi.2016.10.013 (2017). [PubMed: 27984203]

45. Garlid KD, Orosz DE, Modriansky M, Vassanelli S & Jezek P On the mechanism of fatty acid-induced proton transport by mitochondrial uncoupling protein. J Biol Chem 271, 2615–2620 (1996). [PubMed: 8576230]

46. Pebay-Peyroula E et al. Structure of mitochondrial ADP/ATP carrier in complex with carboxyatractyloside. Nature 426, 39–44 (2003). [PubMed: 14603310]

47. Esposito LA, Melov S, Panov A, Cottrell BA & Wallace DC Mitochondrial disease in mouse results in increased oxidative stress. Proc Natl Acad Sci U S A 96, 4820–4825 (1999). [PubMed: 10220377]

48. Gadd ME et al. Mitochondrial iPLA2 activity modulates the release of cytochrome c from mitochondria and influences the permeability transition. J Biol Chem 281, 6931–6939, doi:M510845200 [pii]10.1074/jbc.M510845200 (2006). [PubMed: 16407316]

49. Kinsey GR, McHowat J, Beckett CS & Schnellmann RG Identification of calcium-independent phospholipase A2gamma in mitochondria and its role in mitochondrial oxidative stress. Am J Physiol Renal Physiol 292, F853–860, doi:00318.2006 [pii]10.1152/ajprenal.00318.2006 (2007). [PubMed: 17047165]

50. Burke JE & Dennis EA Phospholipase A2 structure/function, mechanism, and signaling. J Lipid Res 50 Suppl, S237–242, doi:10.1194/jlr.R800033-JLR200 (2009). [PubMed: 19011112]
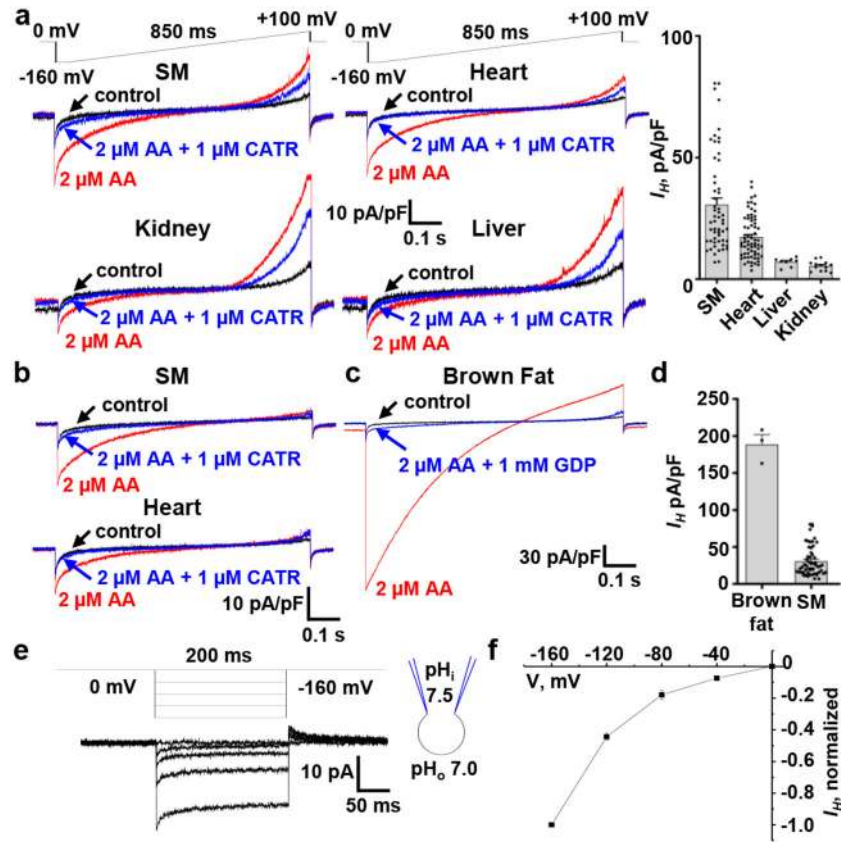
**Figure 1 |. Pharmacological and biophysical properties of $I_H$.**
**a**, $I_H$ induced by 2 μM AA (red) was inhibited by 1 μM CATR (blue) in SM (n=22), heart (n=18), kidney (n=4), and liver (n=7) mitoplasts. *Right panel:* $I_H$ current densities at −160 mV in SM (n=56), heart (n=67), kidney (n=8), and liver (n=13) . Data represent mean±SEM. **b**, Representative recording from SM (upper panel, n=5) and heart (lower panel, n=4) mitoplasts pre-treated with 50 μM mersalyl. $I_H$ induced by 2 μM AA (red) was inhibited by 1 μM CATR (blue). **c**, UCP1-dependent $I_H$ induced by 2 μM AA (red) in brown fat mitoplast (n=3) was inhibited by 1 mM GDP (blue). **d**, Densities of AAC and UCP1 $I_H$ induced by 2 μM AA at −160 mV in SM (n=56) and brown fat (n=3). Data represent mean±SEM. **e**, Representative $I_H$ induced by 2 μM AA at different membrane voltages. Heart mitoplasts, n=4. **f**, Current-voltage (I/V) curve of $I_H$ based on data in (e). Data are mean±SEM.
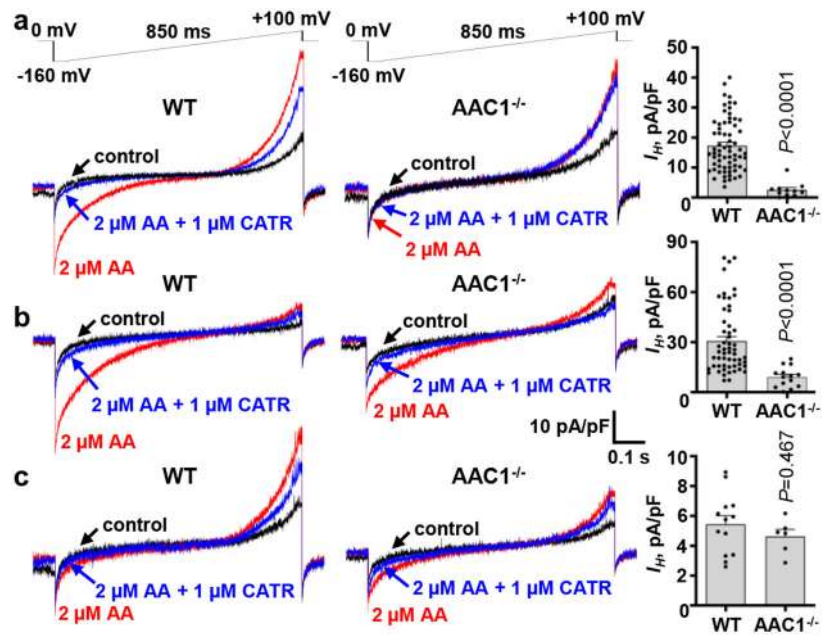
**Figure 2 ∣. AAC is required for $I_H$.**
**a-c**, Representative currents induced by 2 μM AA in WT and $AAC1^{-/-}$ mitoplasts of heart (a), SM (b), and kidney (c). *Right panels: $I_H$* current densities at −160 mV for WT and $AAC1^{-/-}$ mitoplasts. All $AAC1^{-/-}$ experiments used the same WT control as in Fig. 1a. Heart: WT, n=67 and $AAC1^{-/-}$, n=11. SM: WT, n=56 and $AAC1^{-/-}$, n=14. Kidney: WT, n=13 and $AAC1^{-/-}$, n=6. Mann-Whitney test, two-tailed. Data are mean±SEM.
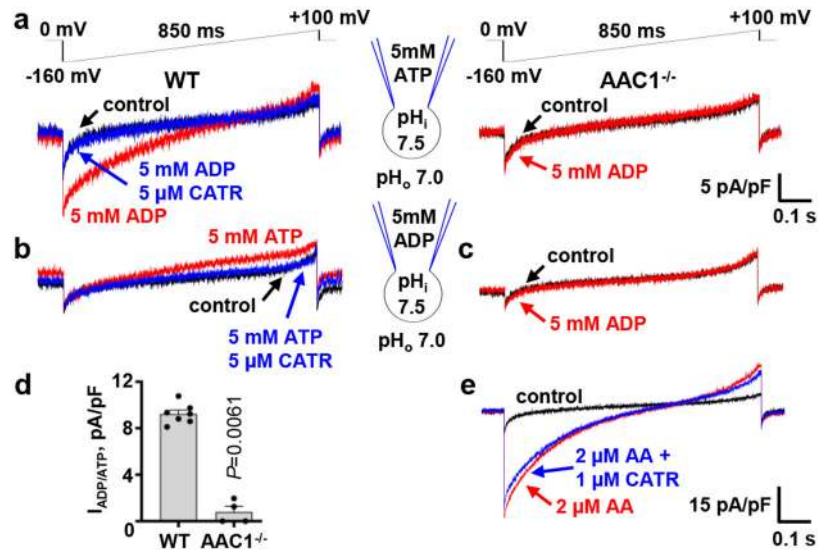
**Figure 3 |. Adenine nucleotide transport by AAC.**

**a**, *Left panel:* AAC current before (control, black) and after (red) addition of 5 mM ADP to the bath solution. Pipette solution contained 5 mM ATP. Subsequent addition of 5 μM CATR (blue) inhibited ADP/ATP exchange. *Right panel:* The same experiment performed in *AAC1$^{-/-}$* mitoplasts. Heart mitoplasts, n=7 (WT), and n=4 (*AAC1$^{-/-}$*). **b**, AAC current before (control, black) and after (red) addition of 5 mM ATP to the bath solution. Pipette solution contained 5 mM ADP. Subsequent addition of 5 μM CATR (blue) inhibited ADP/ATP exchange. Heart mitoplasts, n=5. **c**, Current before (control, black) and after (red) addition of 5 mM ADP to the bath solution. Pipette solution contained 5 mM ADP. Heart mitoplasts, n=3. **d**, Densities of the ADP/ATP exchange current in WT (n=7) and *AAC1$^{-/-}$* (n=4) heart mitoplasts, measured at −160 mV in (a). Mann-Whitney test, two-tailed. Data represent mean±SEM. **e**, $I_H$ activated by 2 μM AA before (red) and after (blue) addition of 1 μM CATR to bath (SM mitoplast). The mitoplast was pretreated with 1 mM ADP just before AA application. Heart and SM mitoplasts, n=7.
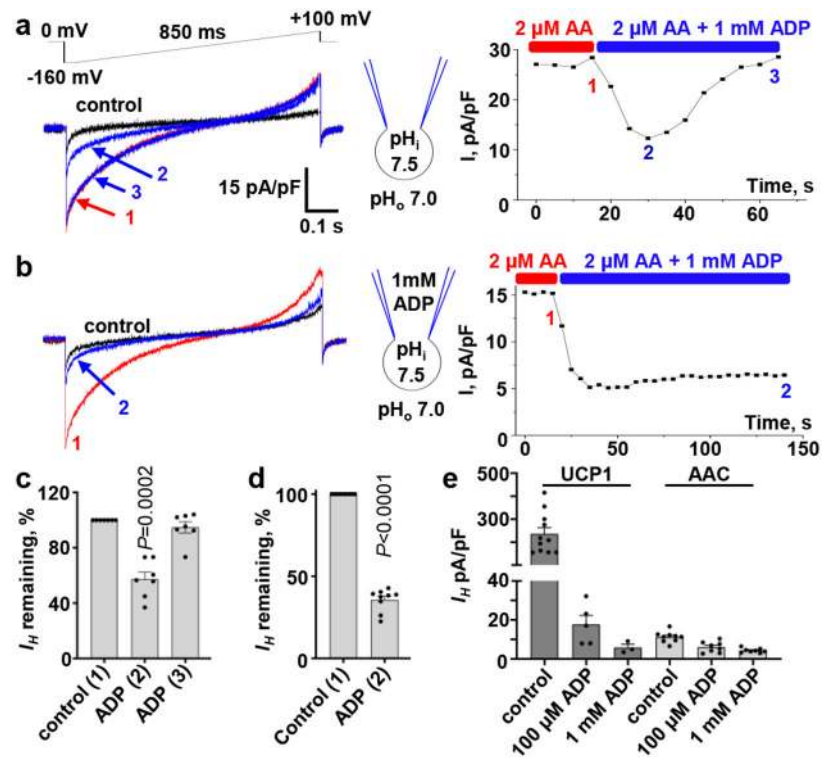
**Figure 4 |.** *Nucleotide exchange negatively regulates $I_H$.*

**a**, *Left panel:* $I_H$ induced by 2 μM AA (1), followed by a transient inhibition by 1 mM of bath ADP (2), and subsequent recovery (3). SM mitoplast. *Right panel:* $I_H$ time course of left panel. $I_H$ was measured at −160 mV. The experiment was repeated with the similar result (n=7) in heart and SM mitoplasts. **b**, *Left panel:* $I_H$ activated by 2 μM AA (red) was inhibited by addition of 1 mM ADP to bath. Pipette solution contained 1 mM ADP. Heart mitoplast. *Right panel:* $I_H$ time course of the left panel. The experiment was repeated with the similar result (n=9) in heart and SM mitoplasts. **c**, ADP inhibition of $I_H$ in points 2 and 3 as in (a). Heart and SM mitoplasts, n=7. Paired t-test, two-tailed. Data are mean±SEM. **d,** ADP inhibition of $I_H$ in point 2 as in (b). Heart and SM mitoplasts, n=9. Paired t-test, two-tailed. Data are mean±SEM. **e,** Mean densities of $I_H$ via UCP1 (dark grey) and AAC (light grey) in control (n=11, UCP1; n=9, AAC) and in the presence of 100 μM (n=5, UCP1; n=8, AAC) and 1 mM ADP (n=3, UCP1; n=8, AAC). $I_H$ was measured as in Extended Data Fig. 9e and f. Brown fat and heart mitoplasts. Data are mean±SEM.
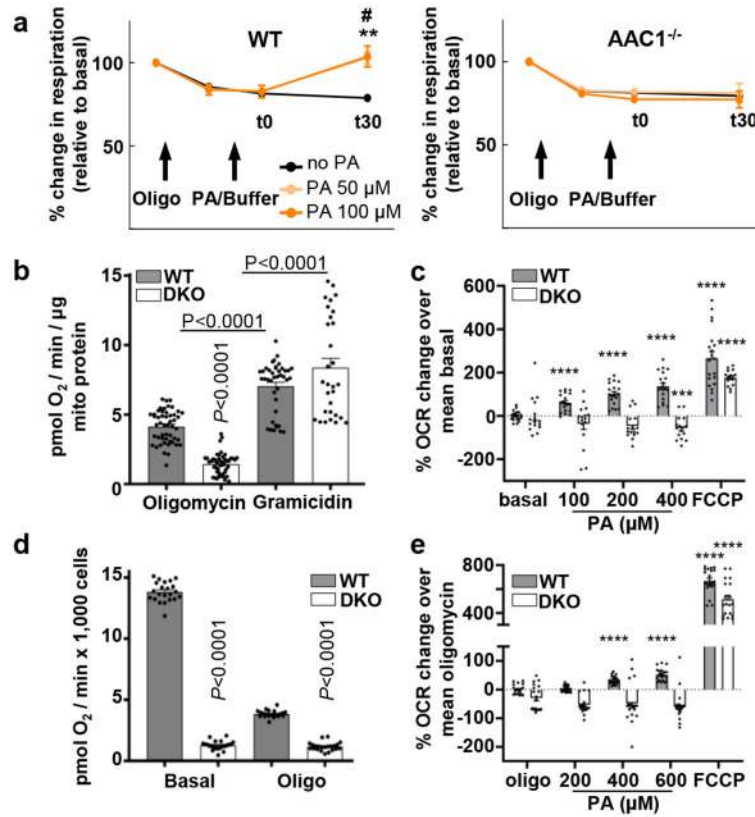
**Figure 5 |. Mitochondrial uncoupling requires AAC.**

**a,** OCR of isolated heart mitochondria of WT (left panel) and $AAC1^{-/-}$ mice (right panel) normalized to the basal value. Arrows indicate addition of oligomycin (Oligo) and either palmitic acid (PA: 50 μM, light orange, n=5 for WT, n=3 for AAC1$^{-/-}$; and 100 μM, dark orange, n=4 for WT, n=3 for AAC1$^{-/-}$) or buffer (black, n=5 for WT, n=3 for AAC1$^{-/-}$). Each n corresponds to independent mitochondrial isolations (also see Methods). The effect of the PA was recorded upon addition (t0) and 30 min later (t30). Paired t-test, two-tailed. **no FA ($P$=0.0009) vs 50 μM PA; #no FA vs 100 μM ($P$=0.0183). Data represent mean ±SEM. **b**, OCR of mitochondria isolated from WT (black) and DKO (grey) C2C12 cells before (basal, oligomycin added; n=50 for WT, and n=47 for DKO) and after addition of gramicidin A (n=40 for WT and n=30 for DKO). Each n corresponds to individual respiration wells. Mann-Whitney test, two-tailed. Data represent mean±SEM. **c**, OCR change in WT (grey, n=20 wells) and DKO (white, n=16 wells) C2C12 isolated mitochondria upon sequential addition of increasing concentrations of PA, and FCCP. All OCR changes were normalized per mean basal OCR (before FA addition). Mann-Whitney test, two-tailed. ***, P=0.0021; ****, P>0.0001 compared to basal. Data represent mean ±SEM. **d,** OCR of WT (black, n=22 wells) and DKO (grey, n=22 wells) C2C12 cells before (basal) and after addition of oligomycin. Mann-Whitney test, two-tailed. Data represent mean±SEM. **e**, OCR change in WT (grey, n=20 wells) and DKO (white, n=19 wells) C2C12 cells after sequential addition of increasing concentrations of PA, and FCCP. All OCR changes were normalized per the mean oligomycin OCR (before FA addition). Mann-

Whitney test, two-tailed. ****, P>0.0001 compared to oligomycin. Data represent mean ±SEM. The growth medium for WT and DKO cell contained 25 mM glucose.